

Portland State University

PDXScholar

Mathematics and Statistics Faculty
Publications and Presentations

Fariborz Maseeh Department of Mathematics
and Statistics

8-3-2017

A Finite Difference Method for Off-fault Plasticity throughout the Earthquake Cycle

Brittany A. Erickson

Portland State University, berickson@pdx.edu

Eric M. Dunham

Stanford University

Arash Khosravifar

Portland State University

Follow this and additional works at: https://pdxscholar.library.pdx.edu/mth_fac



Part of the [Mathematics Commons](#), [Physics Commons](#), and the [Tectonics and Structure Commons](#)

Let us know how access to this document benefits you.

Citation Details

Brittany A. Erickson, Eric M. Dunham, Arash Khosravifar, A Finite Difference Method for Off-fault Plasticity throughout the Earthquake Cycle, *Journal of the Mechanics and Physics of Solids* (2017), doi: 10.1016/j.jmps.2017.08.002

This Post-Print is brought to you for free and open access. It has been accepted for inclusion in Mathematics and Statistics Faculty Publications and Presentations by an authorized administrator of PDXScholar. Please contact us if we can make this document more accessible: pdxscholar@pdx.edu.

A Finite Difference Method for Off-fault Plasticity throughout the Earthquake Cycle

Brittany A. Erickson^a, Eric M. Dunham^{b,c}, Arash Khosravifar^d

^a*Department of Mathematics and Statistics, Portland State University, Portland, OR 97201, USA. berickson@pdx.edu*

^b*Department of Geophysics, Stanford University, Stanford, CA, USA.*

^c*Institute for Computational & Mathematical Engineering, Stanford University, Stanford, CA, USA.*

^d*Department of Civil and Environmental Engineering, Portland State University, Portland, OR, USA.*

Abstract

We have developed an efficient computational framework for simulating multiple earthquake cycles with off-fault plasticity. The method is developed for the classical antiplane problem of a vertical strike-slip fault governed by rate-and-state friction, with inertial effects captured through the radiation-damping approximation. Both rate-independent plasticity and viscoplasticity are considered, where stresses are constrained by a Drucker-Prager yield condition. The off-fault volume is discretized using finite differences and tectonic loading is imposed by displacing the remote side boundaries at a constant rate. Time-stepping combines an adaptive Runge-Kutta method with an incremental solution process which makes use of an elastoplastic tangent stiffness tensor and the return-mapping algorithm. Solutions are verified by convergence tests and comparison to a finite element solution. We quantify how viscosity, isotropic hardening, and cohesion affect the magnitude and off-fault extent of plastic strain that develops over many ruptures. If hardening is included, plastic strain saturates after the first event and the response during subsequent ruptures is effectively elastic. For viscoplasticity without hardening, however, successive ruptures continue to generate additional plastic strain. In all cases, coseismic slip in the shallow sub-surface is diminished compared to slip accumulated at depth during interseismic loading. The evolution of this slip deficit with each subsequent event, however, is dictated by the plasticity model. Integration of the off-fault plastic strain from the viscoplastic model reveals that a significant amount of tectonic off-

Preprint submitted to J. Mech. Phys. Solids

August 16, 2017

set is accommodated by inelastic deformation (~ 0.1 m per rupture, or $\sim 10\%$ of the tectonic deformation budget).

Keywords: earthquake cycle, plasticity, Drucker-Prager, finite difference method

1. Introduction

Field observations reveal regions of highly damaged rock (containing abundant microfractures) surrounding a fault core, which many attribute to thousands of years of seismogenic cycling during which earthquakes shatter the rocks in the vicinity of the fault (*Chester and Logan, 1986; Chester et al., 1993; Shipton et al., 2005; Mitchell and Faulkner, 2009; Faulkner et al., 2010; Ben-Zion and Sammis, 2011*). Understanding how an earthquake will propagate is intimately tied to the evolution of these damage zones. Important and unsolved problems include the relationship between the degree of off-fault yielding and mechanical properties of fault zone material, how damage zones evolve with increasing cumulative slip, and how damage zones affect subsequent rupture.

Current models for dynamic rupture have led to much insight into earthquake propagation, the generation of high-frequency ground motion, and the influence of plasticity on rupture propagation (*Templeton and Rice, 2008; Ma and Andrews, 2010; Dunham et al., 2011a,b; Kaneko and Fialko, 2011; Xu et al., 2012a,b; Shi and Day, 2013; Gabriel et al., 2012, 2013*). Although the inclusion of a plastic material response has been shown to reduce stress and slip velocities at the rupture front to reasonable values, little work has been done to understand the evolution of a damage zone (and its impact on rupture) over multiple event sequences. In particular, most dynamic rupture models currently make the assumption of a uniform background stress and are limited to single-event simulations where rupture is artificially initiated via a stress perturbation imposed on the fault. Earthquake cycle models, on the other hand, generate self-consistent initial conditions because of their ability to handle varying time scales. Cycle models developed in the boundary integral or boundary element context were limited to simulations in a uniform, linear elastic whole- or half-space (*Lapusta et al., 2000; Tullis et al., 2012*). Recent developments, however, have shown how to incorporate more realistic features (material heterogeneities or inelastic deformation, for example) into the earthquake cycle framework (*Johnson and Segall, 2004; Kaneko*

32 *et al.*, 2011; *Barbot et al.*, 2012; *Aagaard et al.*, 2013; *Erickson and Dunham*,
33 2014; *Thompson and Meade*, 2016; *Allison and Dunham*, 2017).

34 In this work we study the role of plasticity throughout the earthquake
35 cycle. The computational method is developed for the classical antiplane
36 problem of a vertical strike-slip fault governed by rate-and-state friction.
37 The off-fault material is idealized as a Drucker-Prager elastic-plastic solid
38 and stresses are constrained by a depth-dependent yield condition. Inertia
39 is approximated with radiation damping. Within the context of a time-
40 stepping method, we solve the resulting equilibrium equation (a nonlinear,
41 elliptic partial differential equation) for the displacement increment.

42 Although computational plasticity is most commonly addressed in a finite
43 element framework, we develop a finite difference method, as the latter is
44 easy to program, efficient, and can be applied in a straightforward manner in
45 order to obtain a numerical approximation to the solution (*Scalerandi et al.*,
46 1999). Recent work in summation-by-parts finite difference methods has
47 furnished high-order accurate schemes that enforce boundary and interface
48 conditions in a stable manner (through the simultaneous-approximation-term
49 technique) (*Kreiss and Scherer*, 1974, 1977; *Nordström et al.*, 2007; *Svärd*
50 *and Nordström*, 2014). These methods provide a framework for proving
51 convergence for linear and nonlinear problems, which is fundamental in order
52 to obtain credible numerical approximations. In this work, an initial analysis
53 is done of the underlying continuum problem to show it satisfies an energy
54 estimate (in this case, dissipation of mechanical energy in the absence of non-
55 trivial boundary conditions or source terms). The computational method
56 then provides a spatial discretization that mimics the energy estimate of the
57 continuum problem and proves stability of the method.

58 The paper is organized as follows: In section 2 we state the continuum
59 problem solved in this work. A rate-and-state frictional fault is embedded in
60 an elastoplastic solid and the equation for static equilibrium is solved within
61 the context of a time-stepping method that imposes remote loading and fault
62 slip (in a manner consistent with a fault friction law), deferring specific de-
63 tails to later sections. Section 3 provides details of the Drucker-Prager model
64 for rate-independent plasticity that defines the constitutive relation (as vis-
65 coplasticity is a straight-forward extension of the associated algorithms, de-
66 tailed in section 7.2). This is described in terms of the material response at
67 a particular point in the solid, and provides a procedure for evolving stress
68 and plastic strain given a history of total strain. Section 4 applies the results
69 of section 3, detailing the derivation of the incremental form of the contin-

70 uum problem of section 2 and obtaining the governing equation solved within
 71 the time-stepping method. In section 5 we show conditions under which the
 72 resulting boundary value problem for the solid satisfies the Drucker stabil-
 73 ity condition. We also establish conservation of the incremental internal
 74 energy in the absence of nontrivial boundary conditions. Section 6 details
 75 the spatial discretization, specifically a finite difference method for variable
 76 coefficients satisfying a summation-by-parts (SBP) rule with weak enforce-
 77 ment of boundary conditions through the simultaneous-approximation-term
 78 (SAT) technique. The combined method will be denoted throughout the
 79 paper as SBP-SAT. We show that the semi-discrete problem using the SBP-
 80 SAT method mimics the energy balance of the continuum problem. In sec-
 81 tion 7 we describe the time stepping method for the overall problem. The
 82 solid displacement, stress, and plastic strain are updated in response to time-
 83 dependent boundary conditions obtained by updating fault slip in a manner
 84 consistent with the friction law. At each time step we solve numerically
 85 the incremental equilibrium equation for the solid using an iterative Newton
 86 procedure with the return mapping algorithm to calculate stresses consistent
 87 with the constitutive theory. The extension of the algorithms to viscoplas-
 88 ticity is also detailed. In section 8 we present convergence tests and compar-
 89 isons with numerical solutions from a finite element code to verify our finite
 90 difference method. In section 9 we apply our method to earthquake cycle
 91 simulations, and conclude in section 10 with a discussion.

92 2. The Continuum Problem

93 In this work we assume two-dimensional antiplane shear deformation. The
 94 equation for static equilibrium in the medium is given by

$$95 \quad \frac{\partial \sigma_{xy}}{\partial y} + \frac{\partial \sigma_{xz}}{\partial z} = 0, \quad (y, z) \in [-L_y, L_y] \times [0, L_z], \quad (1)$$

96 where σ_{xy} and σ_{xz} are the relevant components of the stress tensor σ . The
 97 constitutive relation (Hooke's law) relates stress to elastic strain through the
 98 relations

$$99 \quad \sigma_{xy} = \mu(\gamma_{xy} - \gamma_{xy}^p), \quad (2a)$$

$$100 \quad \sigma_{xz} = \mu(\gamma_{xz} - \gamma_{xz}^p), \quad (2b)$$

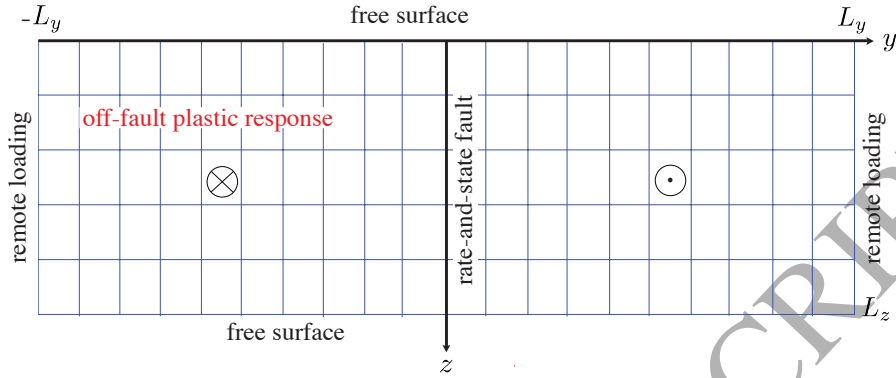


Figure 1: Schematic diagram for antiplane shear deformation where $u(t, y, z)$ is the out-of-plane displacement. We displace the sides $y = \pm L_y$ at a constant rate, with free surface conditions on the top and bottom. A frictional fault at $y = 0$ is embedded in an elastic-plastic medium.

101 for out-of-plane displacement $u(t, y, z)$, shear modulus μ , total engineering
102 strains

$$103 \quad \gamma_{xy} = \partial u / \partial y \quad (3a)$$

$$104 \quad \gamma_{xz} = \partial u / \partial z, \quad (3b)$$

105 and plastic engineering strains $\gamma_{xy}^p, \gamma_{xz}^p$. Plastic deformation evolves according
106 to a flow rule of the form

$$107 \quad \dot{\gamma}_{xy}^p = \lambda P_{xy}, \quad (4a)$$

$$108 \quad \dot{\gamma}_{xz}^p = \lambda P_{xz}, \quad (4b)$$

109 where λ is the magnitude of the plastic strain rate (a positive, scalar function
110 of the stress), which is nonzero only when plastic deformation occurs. P_{xy}, P_{xz}
111 are dimensionless, (generally nonlinear) functions of the stress, determine
112 how the plastic strain rate is partitioned between different components, and
113 specified by the particular plasticity model (*Chen and Han, 1988; Simo and*
114 *Hughes, 1998*). More details are given in section 3.

115 A vertical, strike slip fault governed by a rate-and-state friction law lies
116 at the interface $y = 0$ (*Dieterich, 1979; Ruina, 1983*) (see Figure 1) where
117 we impose the condition that the jump in displacement is equal to the fault
118 slip, Δu , namely

$$119 \quad u(t, 0^+, z) - u(t, 0^-, z) = \Delta u(t, z). \quad (5)$$

120 In addition, we require that the components of the traction vector on the
 121 fault be equal and opposite across the interface, which, for antiplane motion,
 122 reduces to the second interface condition

$$123 \quad \sigma_{xy}(t, 0^+, z) = \sigma_{xy}(t, 0^-, z). \quad (6)$$

124 Slow tectonic loading is imposed by displacing the remote boundaries at a
 125 constant relative rate V_p and the top and bottom boundaries are assumed
 126 to be free surfaces. We assume the solution u is anti-symmetric across the
 127 fault interface (i.e. $u(t, y, z) = -u(t, -y, z)$ for $0 \leq y \leq L_y$) so that (6)
 128 is satisfied by construction, and so we may focus on one side of the fault,
 129 namely $(y, z) \in [0, L_y] \times [0, L_z]$ (see *Erickson and Dunham (2014)* for details
 130 and a discussion on the choice of boundary conditions). For the one-sided
 131 problem the boundary conditions are thus given by

$$132 \quad u(t, 0, z) = \Delta u/2, \quad (7a)$$

$$133 \quad u(t, L_y, z) = V_p t/2, \quad (7b)$$

$$134 \quad \sigma_{xz}(t, y, 0) = 0, \quad (7c)$$

$$135 \quad \sigma_{xz}(t, y, L_z) = 0. \quad (7d)$$

136 In the rate-and-state friction framework, shear stress on the fault, denoted
 137 τ (and related to σ_{xy} as detailed below), is equated with frictional strength
 138 through the relation

$$139 \quad \tau = \sigma_n f(V, \psi), \quad (8)$$

140 where

$$141 \quad V = \Delta \dot{u} \quad (9)$$

142 denotes the slip velocity, ψ is an internal state variable, σ_n is the effective
 143 normal stress and f is a friction coefficient that takes the particular form

$$144 \quad f(V, \psi) = a \sinh^{-1} \left(\frac{V}{2V_0} e^{\psi/a} \right) \quad (10)$$

145 (*Dieterich, 1979; Ruina, 1983*). We assume the state variable ψ evolves to
 146 the aging law form of evolution, namely

$$147 \quad \frac{d\psi}{dt} = \frac{bV_0}{D_c} \left(e^{(f_0 - \psi)/b} - \frac{V}{V_0} \right). \quad (11)$$

148 With the aging law, state can evolve in the absence of slip, and therefore
 149 may be more suitable for modeling the interseismic period. In equations (10)
 150 and (11), a and b are dimensionless parameters quantifying the direct effect
 151 and state evolution, respectively, f_0 is a reference friction at a reference slip
 152 velocity V_0 , and D_c is the state evolution distance (*Marone, 1998*).

153 In section 7 we describe how the slip Δu is obtained in a manner consistent
 154 with the fault friction law (8), where τ is related to σ_{xy} through the following.
 155 Solving the equilibrium equation (1) provides the quasistatic stresses σ_{xy}, σ_{xz} .
 156 Since disregarding inertia entirely is known to cause slip velocity $V \rightarrow \infty$
 157 in finite time (after which no solution exists), we incorporate the radiation
 158 damping approximation to inertia (*Rice, 1993*). Thus τ is defined to be

$$159 \quad \tau = \sigma_{xy}(t, 0, z) - \eta_{rad}V \quad (12)$$

160 where $-\eta_{rad}V$ is the stress due to radiation damping and $\eta_{rad} = \mu/(2c_s)$
 161 is half the shear-wave impedance (not to be confused with viscosity η for
 162 viscoplastic flow) for shear wave speed $c_s = \sqrt{\mu/\rho}$ and material density ρ .

163 3. Elastoplastic Constitutive Theory

164 In this section we review the Drucker-Prager elastoplastic constitutive
 165 theory that is used to evolve stress and plastic strain (in response to an
 166 imposed total strain history at a particular material point).

167 3.1. Drucker-Prager Plasticity

168 Throughout this work we assume infinitesimal strains. Hooke's law (intro-
 169 duced in (2) for the antiplane setting) can be expressed generally by

$$170 \quad \sigma = C : (\epsilon - \epsilon^p) \quad (13)$$

171 where ϵ and ϵ^p are the total and plastic strain tensors. The fourth order
 172 elasticity tensor C_{ijkl} for an isotropic solid is given by

$$173 \quad C_{ijkl} = K\delta_{ij}\delta_{kl} + \mu(\delta_{ik}\delta_{jl} + \delta_{il}\delta_{jk} - (2/3)\delta_{ij}\delta_{kl}), \quad (14)$$

174 where K is the bulk modulus. Stresses in the medium are constrained by a
 175 Drucker-Prager yield condition, see Figure 2. For rate-independent response
 176 with linear, isotropic hardening, the yield function is given by

$$177 \quad F(\sigma, \gamma^p) = \bar{\tau} - (\sigma_Y + h\gamma^p), \quad (15)$$

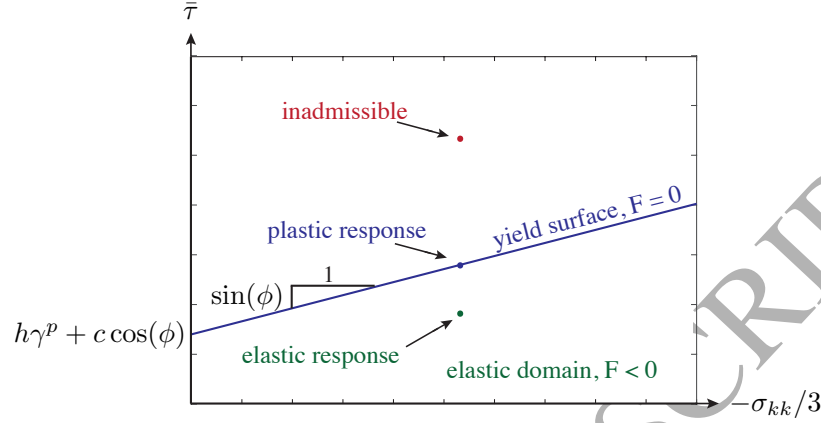


Figure 2: The Drucker-Prager yield condition for yield function F . Elastic response occurs for states of stress that lie below the yield surface, while plastic response occurs for states on the surface. States above the yield surface are inadmissible. The slope of the line is defined by the angle of internal friction ϕ , while the y -intercept depends further on cohesion c and hardening modulus h .

178 where γ^p is the hardening parameter (equivalent plastic strain, defined below)
 179 and h is the hardening modulus. In this work we assume $h > 0$ is constant (we
 180 say the response is strain-softening if $h < 0$, and perfectly plastic if $h = 0$).
 181 The elastic domain in stress space is given by $\mathbb{E}_\sigma = \{(\sigma, \gamma^p) : F(\sigma, \gamma^p) \leq 0\}$
 182 and plastic flow ensues when the yield condition

$$183 \quad F(\sigma, \gamma^p) = 0 \quad (16)$$

184 is met. The second invariant of the deviatoric stress is

$$185 \quad \bar{\tau} = \sqrt{s_{ij}s_{ij}/2} \quad (17)$$

186 for $s_{ij} = \sigma_{ij} - \sigma_{kk}\delta_{ij}/3$. The yield stress is given by

$$187 \quad \sigma_Y = -(\sigma_{kk}/3) \sin \phi + c \cos \phi, \quad (18)$$

188 where c is the cohesion and ϕ is the internal friction angle. Plastic strain
 189 evolves according to the flow rule (introduced in equation (4)) given by

$$190 \quad \dot{\epsilon}_{ij}^p = \lambda P_{ij}, \quad (19)$$

191 where $\lambda = \sqrt{2\dot{e}_{ij}^p \dot{e}_{ij}^p}$ is the deviatoric plastic strain rate for $e_{ij}^p = \epsilon_{ij}^p - \epsilon_{kk}^p \delta_{ij}/3$.

192 Thus

$$193 \quad \gamma^p(t) = \int_0^t \lambda(s) ds, \quad (20)$$

194 and P_{ij} (specified in the next section) quantifies how plastic strain is dis-
195 tributed between different components of the plastic strain rates. The con-
196 stitutive theory is closed by including the Kuhn-Tucker loading/unloading
197 (complementarity) conditions

$$198 \quad \lambda \geq 0, \quad F \leq 0, \quad \lambda F = 0, \quad (21)$$

199 (which ensure that plastic flow can only occur if stresses lie on the yield
200 surface) and the consistency (persistency) condition

$$201 \quad \lambda \dot{F} = 0, \quad (22)$$

202 so that if plastic flow occurs, the stress state must persist on the yield surface
203 for some positive period of time.

204 3.2. Elastoplastic Tangent Stiffness Tensor

205 In rate form, Hooke's law (13) expresses stress rate in terms of total strain
206 rate, namely

$$207 \quad \dot{\sigma}_{ij} = C_{ijkl}^{ep} \dot{\epsilon}_{kl}, \quad (23)$$

208 where the continuum elastoplastic tangent stiffness tensor $C_{ijkl}^{ep} = C_{ijkl}^{ep}(\sigma)$
209 is a nonlinear function of stress. We derive this tensor following *Simo and*
210 *Hughes* (1998), by first taking the time derivative of the yield function, and
211 then using (19) and the time derivative of (20):

$$212 \quad \begin{aligned} \dot{F} = \frac{\partial F}{\partial \sigma_{ij}} \dot{\sigma}_{ij} + \frac{\partial F}{\partial \gamma^p} \dot{\gamma}^p &= \frac{\partial F}{\partial \sigma_{ij}} C_{ijkl} (\dot{\epsilon}_{kl} - \dot{\epsilon}_{kl}^p) + \frac{\partial F}{\partial \gamma^p} \dot{\gamma}^p \\ 213 &= \frac{\partial F}{\partial \sigma_{ij}} C_{ijkl} \dot{\epsilon}_{kl} - \lambda \left(\frac{\partial F}{\partial \sigma_{ij}} C_{ijkl} P_{kl} - \frac{\partial F}{\partial \gamma^p} \right). \end{aligned} \quad (24)$$

214 Assuming that

$$215 \quad \left(\frac{\partial F}{\partial \sigma_{ij}} C_{ijkl} P_{kl} - \frac{\partial F}{\partial \gamma^p} \right) > 0, \quad (25)$$

216 (in order to ensure consistency with (21)-(22), see *Simo and Hughes* (1998)
217 for more details), we can solve $\dot{F} = 0$ for λ , namely

$$218 \quad \lambda = \frac{\langle \frac{\partial F}{\partial \sigma_{ij}} C_{ijkl} \dot{\epsilon}_{kl} \rangle}{\frac{\partial F}{\partial \sigma_{mn}} C_{mnop} P_{op} - \frac{\partial F}{\partial \gamma^p}}, \quad (26)$$

219 where the brackets denote the ramp function $\langle x \rangle = \frac{x+|x|}{2}$. Taking the time
220 derivative of the stress and substituting in the flow rule yields

$$221 \quad \dot{\sigma}_{ij} = C_{ijkl}(\dot{\epsilon}_{kl} - \lambda P_{kl}) = C_{ijkl} \left(\dot{\epsilon}_{kl} - \frac{\langle \frac{\partial F}{\partial \sigma_{mn}} C_{mnop} \dot{\epsilon}_{op} \rangle}{\frac{\partial F}{\partial \sigma_{qr}} C_{qrst} P_{st} - \frac{\partial F}{\partial \gamma^p}} P_{kl} \right), \quad (27)$$

222 which allows us to express the continuum elastoplastic tangent stiffness tensor

$$223 \quad C_{ijkl}^{ep} = \begin{cases} C_{ijkl} & \text{if } \lambda = 0, \\ C_{ijkl} - \frac{C_{ijop} P_{op} C_{mnkl} \frac{\partial F}{\partial \sigma_{mn}}}{\frac{\partial F}{\partial \sigma_{qr}} C_{qrst} P_{st} - \frac{\partial F}{\partial \gamma^p}} & \text{if } \lambda > 0. \end{cases} \quad (28)$$

224 Note that C^{ep} is symmetric in the same manner as the elastic tensor given
225 in (14) (namely, that $C_{ijkl}^{ep} = C_{jikl}^{ep} = C_{ijlk}^{ep} = C_{klij}^{ep}$), if the flow rule (19) is
226 associative (i.e. if $P_{ij} = \frac{\partial F}{\partial \sigma_{ij}}$). For Drucker-Prager plasticity,

$$227 \quad P_{ij} = s_{ij}/(2\bar{\tau}) + (\beta/3)\delta_{ij}, \quad (29)$$

228 where β determines the degree of plastic dilatancy. Thus the flow rule is
229 associative only if $\beta = \sin(\phi)$.

230 Expression (28) is thus

$$231 \quad C_{ijkl}^{ep} = \begin{cases} C_{ijkl} & \text{if } \lambda = 0, \\ C_{ijkl} - \frac{\frac{\mu^2}{\bar{\tau}^2} s_{ij} s_{kl} + \frac{\mu K}{\bar{\tau}} [\sin(\phi) s_{ij} \delta_{kl} + \beta \delta_{ij} s_{kl}] + \beta K^2 \sin(\phi) \delta_{ij} \delta_{kl}}{\mu + \beta K \sin(\phi) + h} & \text{if } \lambda > 0 \end{cases} \quad (30)$$

232 and associativity (symmetry of C_{ijkl}^{ep}) holds in the general case if $\beta = \sin \phi$.

233 4. The Governing Equation in Incremental Form

234 Because of the nonlinearity of the constitutive relation (2), a typical ap-
235 proach taken is to consider the rate form, given by (23), and posit the equi-
236 librium equation (1) in terms of an infinitesimal displacement increment du

237 (*Chen and Han, 1988; Simo and Hughes, 1998; Dunne and Petrinic, 2006*).
 238 In this section we derive the incremental equilibrium equation as well as the
 239 specific forms of the relevant elastoplastic moduli. Note that although du is
 240 an infinitesimally small increment in the continuum setting, it is taken to be
 241 finite when the problem is discretized in time as done in section 7.

242 In the case of antiplane strain, the only non-zero strains are γ_{xy}, γ_{xz} .
 243 For notational purposes, we therefore denote the relevant components of
 244 the fourth-order tensor C as $C_{xyxy} = C_{11}, C_{xyxz} = C_{12}, C_{xzyx} = C_{21}$, and
 245 $C_{xzxz} = C_{22}$. We use similar notation to denote relevant components of the
 246 elastoplastic tangent stiffness tensor, C^{ep} , introduced in the previous section.

247 Using the rate form (23) allows us to replace (2) with an expression solely
 248 in terms of increments of stress $d\sigma$ and strain $d\gamma$, namely

$$249 \quad d\sigma_{xy} = C_{11}^{ep} d\gamma_{xy} + C_{12}^{ep} d\gamma_{xz}, \quad (31a)$$

$$250 \quad d\sigma_{xz} = C_{21}^{ep} d\gamma_{xy} + C_{22}^{ep} d\gamma_{xz}, \quad (31b)$$

251 where

$$252 \quad d\gamma_{xy} = \frac{\partial du}{\partial y}, \quad d\gamma_{xz} = \frac{\partial du}{\partial z} \quad (32)$$

253 are the incremental total engineering strains and du is the (infinitesimal)
 254 displacement increment.

255 Relations (31), along with the strain-displacement relations (32) are substi-
 256 tuted into the incremental form of the equilibrium equation (1) and produce
 257 the nonlinear equilibrium equation for du given by

$$258 \quad \frac{\partial}{\partial y} \left[C_{11}^{ep} \frac{\partial du}{\partial y} + C_{12}^{ep} \frac{\partial du}{\partial z} \right] + \frac{\partial}{\partial z} \left[C_{21}^{ep} \frac{\partial du}{\partial y} + C_{22}^{ep} \frac{\partial du}{\partial z} \right] = 0. \quad (33)$$

259 Recall that the elastoplastic moduli $C_{11}^{ep}, C_{12}^{ep}, C_{21}^{ep}$ and C_{22}^{ep} in equation (33)
 260 depend nonlinearly on the stress. Forming the 2×2 matrix

$$261 \quad \bar{C}^{ep}(\sigma) = \begin{bmatrix} C_{11}^{ep} & C_{12}^{ep} \\ C_{21}^{ep} & C_{22}^{ep} \end{bmatrix} \quad (34)$$

262 (matrix \bar{C} is formed analogously), we derive conditions in section 5 such that
 263 $\det \bar{C}^{ep} > 0$, as is required for well-posedness.

264 Specified background stresses in the medium, denoted $\sigma_{xx}^0, \sigma_{yy}^0, \sigma_{zz}^0$ are
 265 depth variable (see section 9), and the initial background shear stresses are
 266 given by σ_{xy}^0 and σ_{xz}^0 . Note that from (30), antiplane deformation can activate

267 changes in normal stresses (for example, $d\sigma_{xx} = C_{xxxy}^{ep}d\gamma_{xy} + C_{xxxz}^{ep}d\gamma_{xz}$) unless
 268 the relevant components of the tangent stiffness tensor are zero. This scenario
 269 can be avoided with the assumption $\beta = 0$ and $\sigma_{xx}^0 = \sigma_{yy}^0 = \sigma_{zz}^0$, which we
 270 make for the rest of this work.

271 In this work we assume isotropic elastic moduli $C_{11} = C_{22} = \mu$, and
 272 $C_{12} = C_{21} = 0$.

273 For antiplane strain the specific components for the elastoplastic stiffness
 274 tensor (30) are thus

$$275 \quad C_{11}^{ep} = \begin{cases} \mu & \text{if } \lambda = 0, \\ \mu - \frac{\mu\sigma_{xy}^2/\bar{\tau}^2}{1+h/\mu} & \text{if } \lambda > 0, \end{cases} \quad (35)$$

$$276 \quad C_{22}^{ep} = \begin{cases} \mu & \text{if } \lambda = 0, \\ \mu - \frac{\mu\sigma_{xz}^2/\bar{\tau}^2}{1+h/\mu} & \text{if } \lambda > 0, \end{cases} \quad (36)$$

278 and

$$279 \quad C_{12}^{ep} = C_{21}^{ep} = \begin{cases} 0 & \text{if } \lambda = 0, \\ -\frac{\mu\sigma_{xy}\sigma_{xz}/\bar{\tau}^2}{1+h/\mu} & \text{if } \lambda > 0. \end{cases} \quad (37)$$

280 Note that matrix \bar{C}^{ep} is symmetric and in the antiplane setting, Drucker-
 281 Prager reduces to von-Mises plasticity. Equation (17) reduces to

$$282 \quad \bar{\tau} = \sqrt{\sigma_{xy}^2 + \sigma_{xz}^2} \quad (38)$$

283 and the corresponding flow rule (19) is given by

$$284 \quad \dot{\gamma}_{xy}^p = \lambda \frac{\sigma_{xy}}{\bar{\tau}}, \quad \dot{\gamma}_{xz}^p = \lambda \frac{\sigma_{xz}}{\bar{\tau}}. \quad (39)$$

285 The yield stress (18) reduces to

$$286 \quad \sigma_Y = -(\sigma_{kk}^0/3) \sin \phi + c \cos \phi. \quad (40)$$

287 5. Incremental Energy Balance

288 We now switch from tensor notation used in previous sections to matrix/
 289 vector notation, in order to facilitate comparison with the discrete for-
 290 mulation we derive in the next section. We also assume, for ease of the
 291 analysis in the following sections, that the boundary conditions for the in-
 292 cremental problem (33) involve general boundary data dg_L, dg_R, dg_T and dg_B
 293 at the left, right, top and bottom boundaries (respectively) namely,

$$294 \quad du(t, 0, z) = dg_L(t, z), \quad (41a)$$

$$295 \quad du(t, L_y, z) = dg_R(t, z), \quad (41b)$$

$$296 \quad C_{21}^{ep} \frac{\partial du}{\partial y} + C_{22}^{ep} \frac{\partial du}{\partial z} \Big|_{z=0} = dg_T(t, y), \quad (41c)$$

$$297 \quad C_{21}^{ep} \frac{\partial du}{\partial y} + C_{22}^{ep} \frac{\partial du}{\partial z} \Big|_{z=L_z} = dg_B(t, y). \quad (41d)$$

298 Later, however, we outline how we specify incremental boundary conditions
 299 so as to impose fault slip, slow tectonic loading and free surface conditions,
 300 as expressed in (7).

301 Assuming the solution to (33) with boundary conditions (41) is sufficiently
 302 smooth, we multiply (33) by the incremental velocity $d\dot{u}$ and integrate by
 303 parts, yielding the following energy balance

$$304 \quad \frac{d}{dt} dE = \int_0^{L_z} d\dot{u} d\sigma_{xy} \Big|_0^{L_y} dz + \int_0^{L_y} d\dot{u} d\sigma_{xz} \Big|_0^{L_z} dy, \quad (42)$$

305 where the incremental internal energy is defined by

$$306 \quad dE = \frac{1}{2} \int_0^{L_y} \int_0^{L_z} dU^T \bar{C}^{ep}(\sigma) dU dy dz \quad (43)$$

307 for vector

$$308 \quad dU = \begin{bmatrix} \partial du / \partial y \\ \partial du / \partial z \end{bmatrix}.$$

309 The symmetric 2×2 matrix \bar{C}^{ep} has eigenvalues

$$310 \quad \lambda_1, \lambda_2 = \begin{cases} \mu & \text{if } \lambda = 0, \\ \mu, h/(1 + h/\mu) & \text{if } \lambda > 0 \end{cases} \quad (44)$$

311 and (25) implies that $1 + h/\mu > 0$. \bar{C}^{ep} is therefore positive definite for rate-
 312 independent plasticity if and only if $h > 0$ (*Horn and Johnson, 1985*). If
 313 $h < 0$, $\det(\bar{C}^{ep}) = \lambda_1 \lambda_2 \leq 0$, which results in a loss of ellipticity of the equi-
 314 librium equation (33) and a loss of solvability. This case violates Drucker's
 315 first stability postulate (requiring $dU^T \bar{C}^{ep}(\sigma) dU > 0$) and can lead to prob-
 316 lems including loss of uniqueness of the solution (*Drucker, 1959; Jain, 1989*;

317 *Bower, 2010*). For the case $h \leq 0$, the constitutive theory therefore requires
 318 modification (through the introduction of rate dependence, for example).
 319 Thus for rate-independent plasticity, $h > 0$ is required; however, viscosity in
 320 the viscoplastic model ensures a positive definite matrix, even if $h = 0$ (see
 321 section 7.2).

322 Note that in terms of increments, the rate of change of the internal energy
 323 can be decomposed into the sum of the rate of change of the mechanical (elas-
 324 tic strain) energy and the plastic dissipation (a positive quantity), namely,

$$\frac{d}{dt}dE = \frac{d}{dt} \int_0^{L_y} \int_0^{L_z} \frac{1}{2} [dU^e]^T \bar{C} dU^e dy dz + \int_0^{L_y} \int_0^{L_z} [dU^e]^T \bar{C} d\dot{U}^p dy dz, \quad (45)$$

325 where $dU^e = dU - dU^p$, is the vector of elastic strains and the plastic strain
 326 vector is

$$dU^p = \begin{bmatrix} d\gamma_{xy}^p \\ d\gamma_{xz}^p \end{bmatrix}.$$

329 For simplicity in the analysis only (see *Erickson and Dunham (2014)* for
 330 details), we may take the boundary data $dg_L = dg_R = dg_T = dg_B = 0$ and
 331 show that (42) reduces to

$$\frac{d}{dt}dE = 0, \quad (46)$$

333 showing conservation of the incremental internal energy (or dissipation of the
 334 incremental mechanical energy) in the absence of source terms and nontrivial
 335 boundary conditions (i.e., in the absence of work done by body forces or
 336 surface tractions).

337 6. The Spatial Discretization

338 The nonlinearities present in the governing equation (33) with boundary
 339 conditions (41) make analytical solutions difficult, if not impossible to obtain,
 340 except perhaps in certain limiting cases. SBP-SAT finite difference methods
 341 are often used, however, to obtain numerical approximations to solutions
 342 of nonlinear problems (e.g., Navier-Stokes from fluid mechanics (*Nordström*
 343 *et al., 2007*)), although the stability analysis can be challenging and is gen-
 344 erally approached by consideration of the linearized or “frozen coefficient”
 345 problem. If the solution is sufficiently smooth (which is not guaranteed for

our problem), the linearized analysis is often enough to ensure convergence for the nonlinear problem (*Gustafsson, 2008*).

We discretize equation (33) using the second-order accurate, narrow-stencil, summation-by-parts (SBP) finite difference operators for second derivatives, originally defined in *Mattsson and Nordström (2004)* for constant coefficients, and for variable coefficients in *Mattsson (2011)*. Time-dependent boundary conditions are imposed and the elastoplastic moduli C_{11}^{ep} , C_{12}^{ep} , C_{21}^{ep} and C_{22}^{ep} are nonlinear functions of the current stress state (or equivalently, of the displacement increment). We use a Newton's method with line search to solve the nonlinear equation, detailed in section 7.3. At each time step, and each iteration of Newton's method we consider the moduli as frozen, spatially variable coefficients, and use the static counterpart of the spatial discretization of the anisotropic acoustic wave equation in heterogeneous media (*Virta and Mattsson, 2014*).

We apply second-order accurate SBP operators and introduce the 2D operators by first considering one spatial dimension. The 1D domain $y \in [0, L]$ is discretized into $N_y + 1$ grid points y_0, y_1, \dots, y_{N_y} with grid spacing $\Delta y = L/N_y$. First derivatives are approximated by $\frac{\partial u}{\partial y} \approx \mathbf{D}\mathbf{u}$, where $\mathbf{u} = [u_0, u_1, \dots, u_{N_y}]^T$ is the grid function and matrix $\mathbf{D} = \mathbf{H}^{-1}\mathbf{Q}$ is an $N_y + 1 \times N_y + 1$ finite difference operator. \mathbf{H} and \mathbf{Q} are also $N_y + 1 \times N_y + 1$ matrices and the building blocks for the SBP operators. \mathbf{H} is a diagonal, positive definite quadrature matrix defining a discrete norm on the space of grid functions

$$\|\mathbf{u}\|_H^2 = \mathbf{u}^T \mathbf{H} \mathbf{u}, \quad (47)$$

and \mathbf{Q} is an almost skew-symmetric matrix such that $\mathbf{Q} + \mathbf{Q}^T = \text{diag}[-1, 0, 0, \dots, 0, 1]$.

The SBP operators are derived such that they mimic integration-by-parts and provide a discrete energy estimate (that mimics its continuum counterpart). Namely, the relation $\int_0^L u \frac{\partial u}{\partial y} dy = \frac{1}{2} [u^2(L) - u^2(0)]$ is obtained by integration-by-parts and is mimicked discretely by $\mathbf{u}^T \mathbf{H} (\mathbf{D}\mathbf{u}) = \frac{1}{2} \mathbf{u} (\mathbf{Q} + \mathbf{Q}^T) \mathbf{u} = \frac{1}{2} (u_N^2 - u_0^2)$. If $p(y)$ defines the variable coefficient, the narrow-stencil second derivative operator for variable coefficients is given by

$$\frac{\partial}{\partial y} (p(y) \frac{\partial}{\partial y}) \approx \mathbf{D}_2^p = \mathbf{H}^{-1} (-\mathbf{M}^p + \mathbf{pBS}), \quad (48)$$

where $\mathbf{B} = \text{diag}[-1, \dots, 1]$, and \mathbf{S} approximates the first derivative operator on the boundary. Matrix $\mathbf{M}^p = \mathbf{D}^T \mathbf{H} \mathbf{pD} + \mathbf{R}^p$, where $\mathbf{R}^p = \frac{(\Delta y)^3}{4} (\mathbf{D}_2)^T \mathbf{C}_2 \mathbf{pD}_2$

379 (correcting the typographical error in equation (21) in *Erickson and Dunham*
 380 (2014)) is a positive definite damping matrix and $\mathbf{C}_2 = \text{diag}[0, 1, 1, \dots, 1, 1, 0]$
 381 (*Mattsson, 2011*). Matrix $\mathbf{p} = \text{diag}[p(y_0), p(y_1), \dots, p(y_{N_y})]$ is a $N_y + 1 \times$
 382 $N_y + 1$ coefficient matrix (all coefficient matrices are denoted similarly, with
 383 bold notation).

384 In 2D, we discretize the domain $[0, L_y] \times [0, L_z]$ with an $N_y + 1 \times N_z + 1$ -
 385 point grid, defined by

$$386 \quad y_i = i\Delta y, \quad i = 0, 1, \dots, N_y, \quad \Delta y = L_y/N_y, \quad (49a)$$

$$387 \quad z_i = i\Delta z, \quad i = 0, 1, \dots, N_z, \quad \Delta z = L_z/N_z, \quad (49b)$$

388 where Δy and Δz are the grid spacings in each direction. Thus $u_{i,j} \approx$
 389 $u(y_j, z_i)$. Letting $N = (N_y + 1)(N_z + 1)$, the $N \times 1$ grid vector \mathbf{u} in 2D is
 390 given by

$$391 \quad \mathbf{u} = [\mathbf{u}_0^T, \mathbf{u}_1^T, \dots, \mathbf{u}_{N_y}^T] \quad (50)$$

392 where

$$393 \quad \mathbf{u}_i = [u_{0,i}, u_{1,i}, \dots, u_{N_z,i}], \text{ for } i = 0, \dots, N_y. \quad (51)$$

394 The 2D variable coefficient $p(y, z)$ defined on $[0, L_y] \times [0, L_z]$ is transformed
 395 to the $N \times N$ diagonal matrix $\mathbf{p} = \text{diag}[\mathbf{p}_0^T, \mathbf{p}_1^T, \dots, \mathbf{p}_{N_y}^T]$ using analogous
 396 notation. To form the SBP finite difference operators in 2D we make use of
 397 the Kronecker product. Recall that if matrix \mathbf{A} is size $p \times q$ and \mathbf{B} is $r \times s$
 398 then the Kronecker product of the two is of size $pr \times qs$ and given by

$$399 \quad \mathbf{A} \otimes \mathbf{B} = \begin{bmatrix} a_{0,0}\mathbf{B} & \cdots & a_{0,N}\mathbf{B} \\ \vdots & & \vdots \\ a_{N,0}\mathbf{B} & \cdots & a_{N,N}\mathbf{B} \end{bmatrix}. \quad (52)$$

400 In addition, the following identities hold:

$$401 \quad (\mathbf{A} \otimes \mathbf{B})(\mathbf{C} \otimes \mathbf{D}) = (\mathbf{AC}) \otimes (\mathbf{BD}), \quad (53a)$$

$$402 \quad (\mathbf{A} \otimes \mathbf{B})^{-1} = (\mathbf{A}^{-1} \otimes \mathbf{B}^{-1}) \text{ if } \mathbf{A} \text{ and } \mathbf{B} \text{ are invertible,} \quad (53b)$$

$$403 \quad (\mathbf{A} \otimes \mathbf{B})^T = \mathbf{A}^T \otimes \mathbf{B}^T. \quad (53c)$$

404 We can thus extend any 1D operator \mathbf{P} to 2D (in the y and z direction,
 405 respectively) by

$$406 \quad \mathbf{P}_y = (\mathbf{P} \otimes \mathbf{I}), \quad (54a)$$

$$407 \quad \mathbf{P}_z = (\mathbf{I} \otimes \mathbf{P}). \quad (54b)$$

408 The first and second derivative operators in 2D are thus

$$409 \quad \frac{\partial}{\partial y} \approx \mathbf{D}_y, \quad (55a)$$

$$410 \quad \frac{\partial}{\partial z} \approx \mathbf{D}_z, \quad (55b)$$

$$411 \quad \frac{\partial}{\partial y} \left(p(y, z) \frac{\partial}{\partial y} \right) \approx \mathbf{D}_{2y}^p = \mathbf{H}_y^{-1} [-\mathbf{D}_y^T \mathbf{p} \mathbf{H}_y \mathbf{D}_y - \mathbf{R}_y^p + \mathbf{p} \mathbf{B}_y \mathbf{S}_y], \quad (55c)$$

$$412 \quad \frac{\partial}{\partial z} \left(p(y, z) \frac{\partial}{\partial z} \right) \approx \mathbf{D}_{2z}^p = \mathbf{H}_z^{-1} [-\mathbf{D}_z^T \mathbf{p} \mathbf{H}_z \mathbf{D}_z - \mathbf{R}_z^p + \mathbf{p} \mathbf{B}_z \mathbf{S}_z], \quad (55d)$$

413 where $\mathbf{R}_y^p, \mathbf{R}_z^p$ are positive definite damping matrices in 2D (see *Erickson*
414 *and Dunham* (2014) for details). The equilibrium equation (33), along with
415 boundary conditions (41), is thus discretized by

$$416 \quad \mathbf{D}_{2y}^{\mathbf{C}^{ep}} \mathbf{d}\mathbf{u} + \mathbf{D}_y \mathbf{C}_{12}^{ep} \mathbf{D}_z \mathbf{d}\mathbf{u} + \mathbf{D}_z \mathbf{C}_{21}^{ep} \mathbf{D}_y \mathbf{d}\mathbf{u} + \mathbf{D}_{2z}^{\mathbf{C}^{ep}} \mathbf{d}\mathbf{u} + \mathbf{P}_L + \mathbf{P}_R + \mathbf{P}_T + \mathbf{P}_B = \mathbf{0}, \quad (56)$$

417 where $\mathbf{d}\mathbf{u}$ is the incremental displacement grid vector, and the SAT penalty
418 vectors are given by

$$419 \quad \mathbf{P}_L = \mathbf{H}_y^{-1} (\boldsymbol{\alpha}_L + \beta \mathbf{H}_z^{-1} (-\mathbf{C}_{11}^{ep} \mathbf{S}_y - \mathbf{C}_{12}^{ep} \mathbf{D}_z)^T) \mathbf{H}_z \mathbf{E}_0 (\mathbf{d}\mathbf{u}_L - \mathbf{d}\mathbf{g}_L) \quad (57a)$$

$$420 \quad \mathbf{P}_R = \mathbf{H}_y^{-1} (\boldsymbol{\alpha}_R + \beta \mathbf{H}_z^{-1} (\mathbf{C}_{11}^{ep} \mathbf{S}_y + \mathbf{C}_{12}^{ep} \mathbf{D}_z)^T) \mathbf{H}_z \mathbf{E}_N (\mathbf{d}\mathbf{u}_R - \mathbf{d}\mathbf{g}_R) \quad (57b)$$

$$421 \quad \mathbf{P}_T = -\mathbf{H}_z^{-1} (\mathbf{I}_y \otimes \mathbf{E}_0) ([-\mathbf{C}_{22}^{ep} \mathbf{S}_z \mathbf{d}\mathbf{u} - \mathbf{C}_{21}^{ep} \mathbf{D}_y \mathbf{d}\mathbf{u}]_T - \mathbf{d}\mathbf{g}_T) \quad (57c)$$

$$422 \quad \mathbf{P}_B = -\mathbf{H}_z^{-1} (\mathbf{I}_y \otimes \mathbf{E}_N) ([\mathbf{C}_{22}^{ep} \mathbf{S}_z \mathbf{d}\mathbf{u} + \mathbf{C}_{21}^{ep} \mathbf{D}_y \mathbf{d}\mathbf{u}]_B - \mathbf{d}\mathbf{g}_B). \quad (57d)$$

423 Recall that the coefficient matrices in (56) depend nonlinearly on the stress $\boldsymbol{\sigma}$.
424 The notation $\mathbf{d}\mathbf{u}_L$ is the restriction of the grid vector $\mathbf{d}\mathbf{u}$ to the left boundary
425 and $\mathbf{d}\mathbf{u}_R, \mathbf{d}\mathbf{u}_T, \mathbf{d}\mathbf{u}_B$, are the restrictions to the right, top and bottom bound-
426 aries (respectively). Vector $\mathbf{d}\mathbf{g}_L$ is the boundary data dg_L evaluated at the
427 grid and $\mathbf{d}\mathbf{g}_R, \mathbf{d}\mathbf{g}_T, \mathbf{d}\mathbf{g}_B$ are defined analogously. Matrices \mathbf{E}_0 and \mathbf{E}_N map
428 the restricted vectors to full-length ($N \times 1$ length) vectors (see *Erickson and*
429 *Dunham* (2014) for details). *Virta and Mattsson* (2014) derive conditions
430 on the penalty parameter β and penalty matrices $\boldsymbol{\alpha}_L$, and $\boldsymbol{\alpha}_R$ such that a
431 semi-discrete energy estimate can be obtained. Following their analysis, the
432 semi-discrete incremental internal energy $\mathbf{d}\mathbf{E}$ (a slightly modified analog of
433 (43)) is defined

$$434 \quad \mathbf{d}\mathbf{E} = \frac{1}{2} \mathbf{d}\mathbf{U}^T (\mathbf{H}_y \otimes \mathbf{H}_z) \bar{\mathbf{C}}^{ep} \mathbf{d}\mathbf{U} + \frac{1}{2} \mathbf{d}\mathbf{u}^T (\mathbf{R}_y^{\mathbf{C}^{ep}} \otimes \mathbf{H}_z) \mathbf{d}\mathbf{u} + \frac{1}{2} \mathbf{d}\mathbf{u}^T (\mathbf{H}_y \otimes \mathbf{R}_z^{\mathbf{C}^{ep}}) \mathbf{d}\mathbf{u} + U_1 + U_2. \quad (58)$$

435 In (58), vector $\mathbf{dU} = [\mathbf{D}_y \mathbf{d}\mathbf{u} \ \mathbf{D}_z \mathbf{d}\mathbf{u}]^T$, the positive-definiteness of the $2N \times$
 436 $2N$, block diagonal matrix

$$437 \quad \bar{\mathbf{C}}^{ep} = \begin{bmatrix} \mathbf{C}_{11}^{ep} & \mathbf{C}_{12}^{ep} \\ \mathbf{C}_{21}^{ep} & \mathbf{C}_{22}^{ep} \end{bmatrix} \quad (59)$$

438 follows from that of $\bar{\mathbf{C}}^{ep}$, and U_1, U_2 are positive quantities, see Appendix
 439 A. Assuming zero-boundary data, as in the continuum problem, the semi-
 440 discrete equations are shown to satisfy the energy estimate

$$441 \quad \frac{d}{dt} \mathbf{dE} \leq 0, \quad (60)$$

442 which ensures stability of the method, see Appendix A for more details. Note
 443 that for our application problems in section 9 we desire better resolution near
 444 the fault and free surface, and therefore consider a non-uniform grid spacing.
 445 In appendix A we detail the stability analysis for a grid with non-uniform
 446 spacing; the uniform grid spacing assumed in this section (to maintain flow
 447 of the discussion) is a special case.

448 7. Time Stepping

449 In this section we explain the time stepping method for the overall prob-
 450 lem. This is done by first updating slip and the state variable along the
 451 frictional fault. The update to slip, along with the remaining boundary con-
 452 ditions, generates an increment of load. Updates to the displacement, stresses
 453 and plastic strains (that occur in the volume in response to the load) are then
 454 computed.

455 We introduce a time discretization so that notationally, superscripts on
 456 a particular field imply we are considering a *finite* increment over a discrete
 457 time step. We assume the system is equilibrated at time t^n with stresses con-
 458 sistent with the constitutive theory of section 3. Slip and state variable along
 459 the fault are updated via a Runge-Kutta method with adaptive time stepping
 460 (see section 7.4 for details). These updates provide the incremental bound-
 461 ary data $\mathbf{d}\mathbf{g}_L^{n+1}$ along the fault, which, together with $\mathbf{d}\mathbf{g}_R^{n+1}, \mathbf{d}\mathbf{g}_T^{n+1}, \mathbf{d}\mathbf{g}_B^{n+1}$,
 462 correspond to an increment of load applied over the time step $dt = t^{n+1} - t^n$
 463 that drives the system to a new state. In what follows, we describe the lat-
 464 ter part update, namely, how the displacement increment and the associated

465 stresses and plastic strains are updated in response to the load in a manner
466 that accounts for plastic response.

467 Let the discrete equilibrium equation (56)-(57) be denoted $\mathcal{E}(\mathbf{d}\boldsymbol{\sigma}) = \mathbf{b}$
468 where vector \mathbf{b} stores the incremental boundary data. At t^{n+1} we wish to
469 obtain both stress and displacement increments that satisfy

$$470 \quad \mathcal{E}(\mathbf{d}\boldsymbol{\sigma}^{n+1}) = \mathbf{b}^{n+1} \quad (61)$$

471 and are consistent with the constitutive theory of section 3, where $\mathbf{d}\boldsymbol{\sigma}^{n+1}$
472 is related to the displacement increment $\mathbf{d}\mathbf{u}^{n+1}$ through a discrete form of
473 constitutive relation (31) (which we define shortly) and the discretized strain-
474 displacement relations (32).

475 To obtain the displacement, stresses and strains at time t^{n+1} we first
476 apply a backward-Euler discretization to the flow rule (19) and equivalent
477 plastic strain

$$478 \quad \gamma_{xy}^{p,n+1} = \gamma_{xy}^{p,n} + \mathbf{d}\lambda^{n+1} \frac{\boldsymbol{\sigma}^{n+1}_{xy}}{\bar{\tau}^{n+1}} \quad (62a)$$

$$479 \quad \gamma_{xz}^{p,n+1} = \gamma_{xz}^{p,n} + \mathbf{d}\lambda^{n+1} \frac{\boldsymbol{\sigma}^{n+1}_{xz}}{\bar{\tau}^{n+1}}, \quad (62b)$$

$$480 \quad \gamma^{p,n+1} = \gamma^{p,n} + \mathbf{d}\lambda^{n+1}, \quad (62c)$$

481 where $\mathbf{d}\lambda^{n+1} = \lambda^{n+1} dt$. A direct linearization of this discretization implies
482 an associated discrete, incremental form of the constitutive relation given by

$$483 \quad \mathbf{d}\boldsymbol{\sigma}_{ij}^{n+1} = \mathbf{C}_{ijkl}^{ep}(\boldsymbol{\sigma}^{n+1}) \mathbf{d}\boldsymbol{\epsilon}_{kl}^{n+1} \quad (63)$$

484 where \mathbf{C}^{ep} is the *consistent* tangent stiffness tensor (and a function of the
485 stress at the end of the time step), derived in the next section. The fully
486 discrete equilibrium equation can thus be expressed

$$487 \quad \mathcal{E}(\mathbf{C}^{ep}(\boldsymbol{\sigma}^{n+1}) \mathbf{d}\mathbf{u}^{n+1}) = \mathbf{b}^{n+1}, \quad (64)$$

488 and is a nonlinear function of $\mathbf{d}\mathbf{u}^{n+1}$.

489 To solve (64) we proceed via a Newton-type method which utilizes the
490 partial derivative

$$491 \quad \frac{\partial \mathcal{E}}{\partial \mathbf{d}\mathbf{u}^{n+1}} = \frac{\partial \mathcal{E}}{\partial \mathbf{d}\boldsymbol{\sigma}_{ij}^{n+1}} \mathbf{C}_{ijkl}^{ep}(\boldsymbol{\sigma}^{n+1}) \frac{\partial \mathbf{d}\boldsymbol{\epsilon}_{kl}^{n+1}}{\partial \mathbf{d}\mathbf{u}^{n+1}} \quad (65)$$

492 and incorporates the consistent tangent stiffness tensor. We set iteration
 493 index $k = 0$ and compute an initial, elastic guess $\mathbf{du}^{n+1,(k)}$ to the displace-
 494 ment increment, obtained by assuming $\mathcal{C}^{ep} = \mathbf{C}$ and solving (64). Consistent
 495 stresses $\boldsymbol{\sigma}^{n+1,(k)}$ associated with $\mathbf{du}^{n+1,(k)}$ are obtained from the *return map-*
 496 *ping algorithm* which is based on the backward Euler discretization (62), and
 497 detailed in the next section. Deferring specific details until section 7.4, if
 498 the new, consistent stress state satisfies equilibrium, then the final fields are
 499 those at iteration k , and the process is considered done.

500 If equilibrium is not satisfied, however, the displacement increment $\mathbf{du}^{n+1,(k)}$
 501 must be adjusted (and thus adjustments to the stress and plastic strains must
 502 be made).

503 The displacement increment is updated by solving (64) via an iterative
 504 Newton-type method that solves the *linearized* equilibrium problem

$$505 \quad \mathcal{E}(\mathcal{C}^{ep}(\boldsymbol{\sigma}^{n+1,(k)})\mathbf{du}^{n+1,(k+1)}) = \mathbf{b}^{n+1}. \quad (66)$$

506 and the return mapping algorithm provides associated consistent stresses
 507 $\boldsymbol{\sigma}^{n+1,(k+1)}$ (*Simo and Hughes, 1998; de Souza Neto et al., 2008*). This
 508 iterative procedure continues until equilibrium has been satisfied with an
 509 appropriate convergence criterion met (see section 7.3). The displacement
 510 $\mathbf{u}^{n+1} = \mathbf{u}^n + \mathbf{du}^{n+1}$ can then be formed from the converged value of the finite
 511 increment \mathbf{du}^{n+1} .

512 7.1. The Return Mapping Algorithm

513 Within the Newton iteration described in the previous section, the finite
 514 displacement increment $\mathbf{du}^{n+1,(k)}$ is obtained and stresses consistent with the
 515 plastic constitutive theory must be updated (*Simo and Hughes, 1998*). In
 516 this section we describe how to obtain $\boldsymbol{\sigma}^{n+1,(k)}$. First, the strains associated
 517 with $\mathbf{du}^{n+1,(k)}$ are computed

$$518 \quad \gamma_{xy}^{n+1,(k)} = \gamma_{xy}^n + \mathbf{d}\gamma_{xy}^{n+1,(k)}, \quad (67a)$$

$$519 \quad \gamma_{xz}^{n+1,(k)} = \gamma_{xz}^n + \mathbf{d}\gamma_{xz}^{n+1,(k)}, \quad (67b)$$

520 and allow us to compute the elastic trial state (denoted with asterisk *)

$$521 \quad \boldsymbol{\gamma}^{*,p,n+1,(k)} = \boldsymbol{\gamma}^{p,n}, \quad (68a)$$

$$522 \quad \boldsymbol{\sigma}_{xz}^{*,n+1,(k)} = \mu(\boldsymbol{\gamma}_{xz}^{n+1,(k)} - \boldsymbol{\gamma}_{xz}^{p,n}) = \boldsymbol{\sigma}_{xz}^n + \mu\mathbf{d}\boldsymbol{\gamma}_{xz}^{n+1,(k)}, \quad (68b)$$

$$523 \quad \boldsymbol{\sigma}_{xy}^{*,n+1,(k)} = \mu(\boldsymbol{\gamma}_{xy}^{n+1,(k)} - \boldsymbol{\gamma}_{xy}^{p,n}) = \boldsymbol{\sigma}_{xy}^n + \mu\mathbf{d}\boldsymbol{\gamma}_{xy}^{n+1,(k)}, \quad (68c)$$

524 assuming no additional plastic strain has accrued over the time step.

525 The final stress state at time t^{n+1} must satisfy $F \leq 0$, where the yield
526 function is defined in (15) for yield stress (40). If the elastic trial stresses sat-
527 isfy $F \leq 0$, then they are accepted as the final stresses. If the trial stresses lie
528 outside the yield surface ($F > 0$), however, they are be “mapped back” onto
529 the yield surface by adjusting the plastic strains so that $F(\boldsymbol{\sigma}^{n+1}, (k), \boldsymbol{\gamma}^{p,n+1,(k)}) =$
530 0 is satisfied (*Simo and Hughes*, 1998).

531 Substituting equations (62a-b) into (68b-c) yields

$$532 \quad \boldsymbol{\sigma}_{xy}^{*,n+1} = \boldsymbol{\sigma}_{xy}^{n+1} (1 + \mu \mathbf{d}\boldsymbol{\lambda}^{n+1} / \bar{\tau}^{n+1}) \quad (69a)$$

$$533 \quad \boldsymbol{\sigma}_{xz}^{*,n+1} = \boldsymbol{\sigma}_{xz}^{n+1} (1 + \mu \mathbf{d}\boldsymbol{\lambda}^{n+1} / \bar{\tau}^{n+1}). \quad (69b)$$

534 From (69) we calculate

$$535 \quad \begin{aligned} \bar{\tau}^{*,n+1} &= \sqrt{(\boldsymbol{\sigma}_{xy}^{*,n+1})^2 + (\boldsymbol{\sigma}_{xz}^{*,n+1})^2} \\ &= \bar{\tau}^{n+1} + \mu \mathbf{d}\boldsymbol{\lambda}^{n+1}. \end{aligned} \quad (70)$$

537 Re-arranging (70), noting that $F(\boldsymbol{\sigma}^{n+1}, \boldsymbol{\gamma}^{p,n+1}) = 0$, and substituting in (62c)
538 yields the plastic consistency condition

$$539 \quad \mathbf{d}\boldsymbol{\lambda}^{n+1} = F(\boldsymbol{\sigma}^{*,n+1}, \boldsymbol{\gamma}^{*,p,n+1}) / (h + \mu), \quad (71)$$

540 where $\boldsymbol{\gamma}^{*,p,n+1}$ is given by (68c). Finally, solving (69) for $\boldsymbol{\sigma}_{xy}^{n+1}$ and $\boldsymbol{\sigma}_{xz}^{n+1}$
541 yields

$$542 \quad \boldsymbol{\sigma}_{xy}^{n+1,(k)} = \frac{\boldsymbol{\sigma}_{xy}^{*,n+1,(k)}}{1 + \mu \mathbf{d}\boldsymbol{\lambda}^{n+1,(k)} / \bar{\tau}^{n+1,(k)}} = \frac{\boldsymbol{\sigma}_{xy}^{*,n+1,(k)} (\bar{\tau}^{*,n+1,(k)} - \mu \mathbf{d}\boldsymbol{\lambda}^{n+1,(k)})}{\bar{\tau}^{*,n+1,(k)}} \quad (72a)$$

$$543 \quad \boldsymbol{\sigma}_{xz}^{n+1,(k)} = \frac{\boldsymbol{\sigma}_{xz}^{*,n+1,(k)}}{1 + \mu \mathbf{d}\boldsymbol{\lambda}^{n+1,(k)} / \bar{\tau}^{n+1,(k)}} = \frac{\boldsymbol{\sigma}_{xz}^{*,n+1,(k)} (\bar{\tau}^{*,n+1,(k)} - \mu \mathbf{d}\boldsymbol{\lambda}^{n+1,(k)})}{\bar{\tau}^{*,n+1,(k)}} \quad (72b)$$

544 which expresses the final stress state entirely in terms of the computed elastic
545 trial stresses.

546 The consistent elastoplastic tangent stiffness tensor \mathbf{C}_{ijkl}^{ep} in (64) is ob-
547 tained by a linearization of the return-mapping algorithm. We derive these
548 consistent moduli in Appendix B, with specific components (ommitting su-
549 perscripts $n + 1$) given by (bold face notation is not used as these moduli are
550 derived independently of a spatial discretization)

$$551 \quad \mathbf{C}_{11}^{ep} = \begin{cases} \mu & \text{if } \lambda = 0, \\ \mu - \frac{\mu \sigma_{xy}^2 / \bar{\tau}^2}{1+h/\mu} - \frac{d\lambda \mu^2}{\bar{\tau}} \left[1 - \left(\frac{\sigma_{xy}}{\bar{\tau}} \right)^2 \right] & \text{if } \lambda > 0, \end{cases} \quad (73)$$

552

553

$$\mathcal{C}_{22}^{ep} = \begin{cases} \mu & \text{if } \lambda = 0, \\ \mu - \frac{\mu\sigma_{xz}^2/\bar{\tau}^2}{1+h/\mu} - \frac{d\lambda\mu^2}{\bar{\tau}} \left[1 - \left(\frac{\sigma_{xz}}{\bar{\tau}} \right)^2 \right] & \text{if } \lambda > 0, \end{cases} \quad (74)$$

554 and

555

$$\mathcal{C}_{12}^{ep} = \mathcal{C}_{21}^{ep} = \begin{cases} 0 & \text{if } \lambda = 0, \\ -\frac{\mu\sigma_{xy}\sigma_{xz}/\bar{\tau}^2}{1+h/\mu} - \frac{d\lambda\mu^2}{\bar{\tau}} \left[1 - \frac{\sigma_{xy}\sigma_{xz}}{\bar{\tau}^2} \right] & \text{if } \lambda > 0, \end{cases} \quad (75)$$

556 which agree with the continuum moduli in the limit that $d\lambda \rightarrow 0$.

557

558

559

560

561

562

563

564

It has been shown for many problems that using the consistent tangent moduli (73)-(75) with discretization (64) (to compute numerical solutions to (33)) then the quadratic convergence rate typical of Newton-type iterative methods is achieved. This rate of convergence is often lost, however, if the continuum tangent moduli (35)-(37) are used instead (*Simo and Taylor, 1985*). In our application problems we thus use the consistent elastoplastic moduli and leave the comparison of Newton convergence results to future work.

565

7.2. Extension to Viscoplasticity

566

567

568

569

570

571

Classical Perzyna viscoplasticity (*Perzyna, 1966, 1971*) is obtained from rate-independent plasticity by replacing the yield condition (16) with $F(\boldsymbol{\sigma}, \boldsymbol{\gamma}^p) = \eta \boldsymbol{\lambda}$, where $\eta > 0$ is the viscosity.

A viscoplastic response alters the return mapping algorithm in the previous section through the following: If the computed elastic trial stresses are such that $F(\boldsymbol{\sigma}^{*,n+1}, \boldsymbol{\gamma}^{*,p,n+1}) > 0$, then equations (70) and (71) are replaced with

572

$$\bar{\tau}^{*,n+1} = \bar{\tau}^{n+1} + \mu \frac{F^{n+1}}{\eta} dt \quad (76)$$

573 and

574

$$d\boldsymbol{\lambda}^{n+1} = F(\boldsymbol{\sigma}^{*,n+1}, \boldsymbol{\gamma}^{*,p,n+1}) / (\eta/dt + h + \mu). \quad (77)$$

575

576

The consistent elastoplastic tangent moduli (73)-(75) can also be derived from linearizing the return-mapping algorithm (see Appendix B), yielding

$$\mathcal{C}_{11}^{ep} = \begin{cases} \mu & \text{if } \boldsymbol{\lambda} = 0, \\ \mu - \frac{\frac{\mu\sigma_{xy}^2/\bar{\tau}^2}{\eta/dt + 1 + h/\mu}}{\eta/dt + 1 + h/\mu} - \frac{d\lambda\mu^2}{\bar{\tau}} \left[1 - \left(\frac{\sigma_{xy}}{\bar{\tau}} \right)^2 \right] & \text{if } \boldsymbol{\lambda} > 0, \end{cases} \quad (78)$$

$$\mathcal{C}_{22}^{ep} = \begin{cases} \mu & \text{if } \lambda = 0, \\ \mu - \frac{\mu\sigma_{xz}^2/\bar{\tau}^2}{\frac{\eta/\mu}{dt} + 1 + h/\mu} - \frac{d\lambda\mu^2}{\bar{\tau}} \left[1 - \left(\frac{\sigma_{xz}}{\bar{\tau}}\right)^2 \right] & \text{if } \lambda > 0, \end{cases} \quad (79)$$

577 and

$$\mathcal{C}_{12}^{ep} = \mathcal{C}_{21}^{ep} = \begin{cases} 0 & \text{if } \lambda = 0, \\ -\frac{\mu\sigma_{xy}\sigma_{xz}/\bar{\tau}^2}{\frac{\eta/\mu}{dt} + 1 + h/\mu} - \frac{d\lambda\mu^2}{\bar{\tau}} \left[1 - \frac{\sigma_{xy}\sigma_{xz}}{\bar{\tau}^2} \right] & \text{if } \lambda > 0. \end{cases} \quad (80)$$

578 Note that for a fixed η , if $dt \rightarrow 0$, the consistent elastoplastic moduli (78) -
579 (80) approach the elastic moduli. Furthermore, for $\eta > 0$, we can take $h = 0$
580 and still guarantee that $\bar{\mathcal{C}}^{ep}$ is positive definite.

581 7.3. Newton Iteration with Return-Mapping

582 We let $k = 0$, $\mathbf{du}^{n+1,(k)}$ be the initial (elastic) guess for the displacement
583 increment \mathbf{du}^{n+1} , and iterate as follows.

584 Step 1: Compute the strain increments

$$585 \quad \mathbf{d}\gamma_{xy}^{n+1,(k)} = \mathbf{D}_y \mathbf{du}^{n+1,(k)}, \quad (81a)$$

$$586 \quad \mathbf{d}\gamma_{xz}^{n+1,(k)} = \mathbf{D}_z \mathbf{du}^{n+1,(k)}. \quad (81b)$$

587 Step 2: Compute the elastic trial state and use the return mapping algorithm
588 to obtain the consistent stresses $\boldsymbol{\sigma}_{xy}^{n+1,(k)}$, $\boldsymbol{\sigma}_{xz}^{n+1,(k)}$ and plastic strain $\boldsymbol{\gamma}^{p,n+1,(k)}$.

589 Step 3: Check if equilibrium is sufficiently satisfied. That is, check if a
590 stopping criterion is met, for example, $\|\mathcal{E}(\mathcal{C}^{ep}(\boldsymbol{\sigma}^{n+1,(k)})\mathbf{du}^{n+1,(k)}) - \mathbf{b}^{n+1}\| <$
591 tol , where tol is a specified tolerance. If so, set $\mathbf{u}^{n+1} = \mathbf{u}^n + \mathbf{du}^{n+1,(k)}$,
592 the remaining fields are those at iteration (k) , and the Newton iteration
593 is complete. Otherwise set $k = k + 1$, solve $\mathcal{E}(\mathcal{C}^{ep}(\boldsymbol{\sigma}^{n+1,(k)})\mathbf{du}^{n+1,(k+1)}) =$
594 \mathbf{b}^{n+1} for $\mathbf{du}^{n+1,(k+1)}$ and return to step 1, iterating until the Newton method
595 converges and equilibrium is met.

596 7.4. Time Stepping Method

597 In this section we provide details of time stepping for the overall prob-
598 lem, which includes details of the update to slip and the state variable along
599 the fault, and provides an initial guess for the off-fault fields. As stated in
600 section 2, rate-and-state friction, as used in our algorithm, provides the set
601 of differential equations (9)-(11) that are used to evolve the fault boundary
602 displacement (i.e., fault slip). We modify the method from *Erickson and*
603 *Dunham* (2014) in order to incorporate off-fault plasticity. Bold-face type is

604 again used to denote spatially discrete quantities. We assume the body is
 605 equilibrated (with consistent stresses) at time t^n and that \mathbf{V}^n and $\boldsymbol{\psi}^n$ are
 606 known. The following time-stepping method is illustrated in the context of a
 607 forward Euler step, but we use Matlab's adaptive, fourth order Runge-Kutta
 608 method with a relative tolerance of 10^{-7} .

609

610 Step 1. Update slip and state on the fault by explicitly integrating

$$611 \quad \Delta \mathbf{u}^{n+1} = \Delta \mathbf{u}^n + dt \mathbf{V}^n \quad (82a)$$

$$612 \quad \boldsymbol{\psi}^{n+1} = \boldsymbol{\psi}^n + dt G(\mathbf{V}^n, \boldsymbol{\psi}^n). \quad (82b)$$

Step 2. Set the boundary data in (41):

$$\mathbf{d}\mathbf{g}_L^{n+1} = dt \mathbf{V}^n / 2,$$

$$\mathbf{d}\mathbf{g}_R^{n+1} = dt V_p / 2,$$

$$\mathbf{d}\mathbf{g}_T^{n+1} = \mathbf{d}\mathbf{g}_B^{n+1} = 0,$$

613 form \mathbf{b}^{n+1} and solve for an elastic increment $\mathbf{d}\mathbf{u}^{n+1,(0)}$; i.e., take $\mathcal{C}^{ep} = \mathbf{C}$ and
 614 solve the discrete equation (64).

615

616 Step 3. Correct the initial elastic guess $\mathbf{d}\mathbf{u}^{n+1,(0)}$ by iterating following the
 617 Newton procedure in section 7.3 until convergence is reached, thus obtaining
 618 $\mathbf{u}^{n+1}, \boldsymbol{\sigma}_{xy}^{n+1}, \boldsymbol{\sigma}_{xz}^{n+1}, \boldsymbol{\gamma}_{xy}^{p,n+1}, \boldsymbol{\gamma}_{xz}^{p,n+1}, \boldsymbol{\gamma}^{p,n+1}$.

619

620 Step 4. Compute the shear stress $\boldsymbol{\tau}_{qs}^{n+1} = \boldsymbol{\sigma}_{xy}^{n+1}|_{y=0}$ on the fault.

621

622 Step 5. Equate shear stress with frictional strength $\boldsymbol{\tau}_{qs}^{n+1} - \eta_{rad} \mathbf{V}^{n+1} =$
 623 $\boldsymbol{\sigma}_n f(\mathbf{V}^{n+1}, \boldsymbol{\psi}^{n+1})$ and solve for the updated slip velocity \mathbf{V}^{n+1} (solved using
 624 a local, safe-guarded Newton method) and return to step 1.

625 8. Convergence Tests and Comparison with Finite Element Solu- 626 tion

627 We conduct two studies to verify our numerical method. The first study
 628 is a convergence test of our spatial discretization and time-stepping for an
 629 elastic problem; the second study is a comparison test with a finite element
 630 solution for the same plasticity model.

631 For the first study we proceed with the method of manufactured solutions
 632 and show that our numerical solution is converging to the exact solution at
 633 the correct rate (*Roache, 1998*). The nonlinearity introduced by plasticity
 634 makes this procedure difficult, thus we solve the anisotropic elastic version
 635 by assuming that the elastoplastic moduli do not vary with stress or time,
 636 but rather in space only. We want to check that our incremental procedure
 637 will provide a numerical approximation to the exact solution to the non-
 638 incremental equilibrium equation

$$\frac{\partial}{\partial y} \left[C_{11}^{ep}(y, z) \frac{\partial u}{\partial y} + C_{12}^{ep}(y, z) \frac{\partial u}{\partial z} \right] + \frac{\partial}{\partial z} \left[C_{21}^{ep}(y, z) \frac{\partial u}{\partial y} + C_{22}^{ep}(y, z) \frac{\partial u}{\partial z} \right] = 0, \quad (83)$$

639 where the moduli in (83) are known functions of space. Let the exact displace-
 640 ment (denoted with a hat) to (83) be that given in *Erickson and Dunham*
 641 (2014), namely
 642

$$\hat{u}(t, y, z) = \frac{\delta}{2} K(t) \Phi(y, z) + \frac{V_p t}{2} [1 - \Phi(y, z)] + \frac{\tau^\infty}{\mu} y, \quad (84)$$

644 which provides the exact (elastic) stresses (also denoted with hats)

$$\hat{\sigma}_{xy} = C_{11}^{ep}(y, z) \partial \hat{u} / \partial y + C_{12}^{ep}(y, z) \partial \hat{u} / \partial z \quad (85a)$$

$$\hat{\sigma}_{xz} = C_{21}^{ep}(y, z) \partial \hat{u} / \partial y + C_{22}^{ep}(y, z) \partial \hat{u} / \partial z. \quad (85b)$$

647 Appropriate source terms are added to (83) so that \hat{u} is indeed the solu-
 648 tion. In the construction of the exact solution (84), $K(t)$ controls the time-
 649 dependency of the solution, δ is the total slip that occurs during the event,
 650 τ^∞ is a parameter that defines the remote stress, and Φ describes the spatial
 651 dependency of the solution. The specific forms are given by

$$\delta = V_p \bar{t} + V_{\min} \bar{t}, \quad (86a)$$

$$K(t) = \frac{1}{\pi} \left[\tan^{-1} \left(\frac{t - \bar{t}}{t_w} \right) + \frac{\pi}{2} \right] + \frac{V_{\min}}{\delta}, \quad (86b)$$

$$\Phi(y, z) = \frac{H(H + y)}{(H + y)^2 + z^2}, \quad (86c)$$

655 where \bar{t} denotes the event time, t_w denotes the time scale over which the event
 656 occurs, V_{\min} defines a minimum slip velocity throughout the simulation, and

657 H defines a locking depth. For the elastic moduli, we assume the following
658 forms

$$659 \quad C_{11}^{ep} = \mu - \frac{\mu c_1(y, z)^2 / |c|^2}{1 + h/\mu}, \quad (87a)$$

$$660 \quad C_{22}^{ep} = \mu - \frac{\mu c_2(y, z)^2 / |c|^2}{1 + h/\mu}, \quad (87b)$$

$$661 \quad C_{12}^{ep} = C_{21}^{ep} = -\frac{\mu c_1(y, z) c_2(y, z) / |c|^2}{1 + h/\mu}, \quad (87c)$$

662 where

$$663 \quad c_1(y, z) = \frac{H_1^2}{H_1^2 + z^2} \frac{L_1^2}{L_1^2 + y^2}, \quad (88a)$$

$$664 \quad c_2(y, z) = \frac{H_2^2}{H_2^2 + z^2} \frac{L_2^2}{L_2^2 + y^2} \quad (88b)$$

665 and $|c|^2 = c_1^2 + c_2^2$. Thus the moduli form a symmetric, positive definite
666 matrix \bar{C}^{ep} if $h > 0$. The exact slip along the fault is

$$667 \quad \Delta \hat{u}(t, z) = 2\hat{u}(t, 0, z) = \delta K(t) \Phi(0, z) + V_p t [1 - \Phi(0, z)], \quad (89)$$

668 with slip velocity

$$669 \quad \hat{V}(t, z) = \frac{\partial u^*}{\partial t} \Big|_{y=0^+} - \frac{\partial u^*}{\partial t} \Big|_{y=0^-} = \delta K'(t) \Phi(y, z) + V_p [1 - \Phi(0, z)]. \quad (90)$$

670 Lastly, since $\hat{\tau}(t, z) = \hat{\sigma}_{xy}(t, 0, z)$, we can solve (8) for the exact state variable

$$671 \quad \hat{\psi} = a \ln \left[\frac{2V_0}{\hat{V}} \sinh \left(\frac{\hat{\tau} - \eta_{rad} \hat{V}}{\sigma_n a} \right) \right] \quad (91)$$

672 which implies that a source term must also be added to state evolution

$$673 \quad \dot{\psi} = G(V, \psi) + s(t, z) \quad (92)$$

674 where

$$675 \quad s = \dot{\hat{\psi}} - G(\hat{V}, \hat{\psi}). \quad (93)$$

676 All parameter values used in the convergence tests are given in Table 1.
677 At the end of the simulation ($t_f = 70$ years), we compute the relative error

Table 1: Parameters used in the manufactured solution convergence tests.

Parameter	Definition	Value
L_z	fault length	24 km
L_y	off-fault domain length	24 km
ℓ_z	z-length scale for coordinate transform	5 km
ℓ_y	y-length scale for coordinate transform	5 km
H	locking depth	14 km
L_1	y-length scale for c_1	5 km
H_1	z-length scale for c_1	6 km
L_2	y-length scale for c_2	4 km
H_2	z-length scale for c_2	5 km
ρ	density	2670 kg/m ³
μ	shear modulus	30 GPa
h	hardening modulus	30 GPa
σ_n	normal stress on fault	50 MPa
τ^∞	remote shear stress	40 MPa
t_f	final simulation time	70 years
\bar{t}	event nucleation time	35 years
t_w	timescale for event duration	10 s
a	rate-and-state parameter	0.015
b	rate-and-state parameter	0.02
D_c	critical slip distance	0.4 m
V_p	plate rate	10 ⁻⁹ m/s
V_0	reference velocity	10 ⁻⁶ m/s
f_0	reference friction coefficient	0.6

Table 2: Relative error in the discrete \mathbf{H} - and energy-norms with $N = N_x = N_y$. The rate of convergence approaches 2, as expected for a method with second-order accuracy.

N	Error $_H(h)$	Rate	Error $_E(h)$	Rate
2^4	1.030×10^{-3}	–	1.236×10^{-3}	–
2^5	2.867×10^{-4}	1.845	3.514×10^{-4}	1.814
2^6	7.433×10^{-5}	1.947	9.242×10^{-5}	1.927
2^7	1.883×10^{-5}	1.981	2.360×10^{-5}	1.970
2^8	4.741×10^{-6}	1.990	5.967×10^{-6}	1.984

678 between the exact and the numerical approximation in both the discrete
679 H -norm and the energy-norm, defined by

$$680 \quad \text{Error}_H(h) = \|\mathbf{u} - \hat{\mathbf{u}}\|_H / \|\hat{\mathbf{u}}\|_H \quad (94a)$$

$$681 \quad \text{Error}_E(h) = \|\mathbf{u} - \hat{\mathbf{u}}\|_E / \|\hat{\mathbf{u}}\|_E \quad (94b)$$

682 where

$$683 \quad \|\mathbf{u}\|_H^2 = \sum_{i=1}^M \|\mathbf{d}\mathbf{u}_i\|_H^2 \quad (95a)$$

$$684 \quad \|\mathbf{u}\|_E^2 = \sum_{i=1}^M \mathbf{d}\mathbf{E}_i \quad (95b)$$

685 where $\|\mathbf{d}\mathbf{u}\|_H^2 = (\mathbf{d}\mathbf{u})^T (\mathbf{H}_y \otimes \mathbf{H}_z) (\mathbf{d}\mathbf{u})$, M is the number of adaptive, Runge-
686 Kutta time steps and $\mathbf{d}\mathbf{E}$ is the incremental internal energy defined by (58).
687 Table 2 shows that we are achieving second-order convergence, as expected.

688 Because this first verification study confirmed convergence for an anisotropic
689 elastic problem, the purpose of the next study is to validate our results with
690 plasticity. For the second validation study, we compare results of the solution
691 to a boundary value problem subject to Drucker-Prager plasticity. Results
692 from our finite difference code are compared to those from a finite element
693 solution using the OpenSees Software Framework (*Mazzoni et al.*, 2009) and
694 available at <http://opensees.berkeley.edu>.

695 We want to confirm that our incremental approach using equation (33)
696 (in the context of the time stepping method outlined in the previous section)
697 solves the non-incremental form of the governing equation (1), on the domain

698 $(y, z) \in [0, L] \times [0, L]$ with boundary conditions given by

$$699 \quad u(0, z) = 0 \quad (96a)$$

$$700 \quad u(L, z) = g(z) \quad (96b)$$

$$701 \quad \sigma_{xz}(y, 0) = 0 \quad (96c)$$

$$702 \quad \sigma_{xz}(y, L) = 0. \quad (96d)$$

703 Boundary data $g(z)$ and all parameter values are listed in Table 3. Stresses
 704 are subject to the Drucker-Prager yield condition (15) with constant yield
 705 stress σ_Y . We assume an equal grid spacing $\Delta = \Delta y = \Delta z$ of both 1 km
 706 ($N_y = N_z = 24$) and 200 m ($N_y = N_z = 120$). Figure 3 shows solutions
 707 from the finite difference solution to the plastic boundary value problem
 708 with $\Delta = 200$ m, along with the elastic counterpart of the same boundary
 709 value problem, in order to illustrate the differences between the two material
 710 models. Figure 3(a-c) show the displacement and two relevant stress
 711 components of the plastic solution (in dashed lines) and the elastic solution
 712 (solid lines) at different z -values. Figure 3(d-f) are the equivalent fields at
 713 various y -values. Although plasticity mildly affects the displacement field,
 714 the stresses are significantly reduced in amplitude, particularly near $x = 24$
 715 km. Fig. 4 compares contours from the finite difference and finite element
 716 solution with $\Delta = 1$ km. The finite difference solution is plotted in solid
 717 colors, while the finite element solution is plotted with black circles. The
 718 displacement fields in Fig. 4(a-b) are quite similar, but error is visible in the
 719 computed stresses, particularly in Fig. 4(d) near $y = 24$ km. This error is
 720 visibly decreased when mesh refining, as shown in Figure 5. Absolute and rel-
 721 ative errors between the computed fields using the two methods are denoted
 722 by $\text{err}_u^a = \|\mathbf{u}^{FD} - \mathbf{u}^{FE}\|_2$ and $\text{err}_u^r = \|\mathbf{u}^{FD} - \mathbf{u}^{FE}\|_2 / \|\mathbf{u}^{FE}\|_2$, respectively,
 723 and errors for other fields are defined analogously. Results shown in Table 4
 724 suggest the two methods produce similar results.

725 9. Application

726 We are interested in how changes in viscosity, isotropic hardening and
 727 cohesion affect features of the earthquake cycle. We find that all three pa-
 728 rameters influence the magnitude and off-fault extent of plastic strain, and
 729 that in all cases, plasticity affects the amount of slip on the fault in the
 730 shallow sub-surface during each rupture. We use the combined spatial dis-
 731 cretization and time-stepping method detailed in previous sections to sim-

Table 3: Parameters used in antiplane plastic case for comparison of FDM and FEM.

Parameter	Definition	Value
L_z	fault length	24 km
L_y	off-fault domain length	24 km
μ	shear modulus	32.038 GPa
ρ	material density	2670 kg/m ³
$g(z)$	right boundary condition	$-\cos(\pi z/12) + 1$ (m)
σ_Y	yield stress	4 MPa
ϕ	angle of internal friction	0
h	hardening modulus	32.038 GPa

Table 4: Absolute and relative error between our finite difference solution and that obtained from the finite element code in the discrete L^2 -norm for $N_y = N_z = 24, 120$.

N	err_u^a	err_u^r	$\text{err}_{\sigma_{xy}}^a$	$\text{err}_{\sigma_{xy}}^r$	$\text{err}_{\sigma_{xx}}^a$	$\text{err}_{\sigma_{xx}}^r$
24	1.06×10^0	3.27×10^{-2}	1.72×10^0	3.72×10^{-2}	4.76×10^{-2}	3.22×10^{-2}
120	9.87×10^{-2}	3.04×10^{-3}	1.92×10^{-1}	4.14×10^{-3}	3.81×10^{-3}	2.70×10^{-4}

732 ulate multiple earthquake cycles with off-fault plasticity. The fault is gov-
733 erned by rate-and-state friction with depth-variable parameters a and b (see
734 Fig. 6a). Where $a - b < 0$ defines the velocity-weakening (seismogenic)
735 zone, below which the fault creeps interseismically. As an initial study,
736 we assume that the effective normal stresses in the medium are given by
737 $\sigma_{xx}^0 = \sigma_{yy}^0 = \sigma_{zz}^0 = -(\rho - \rho_w)gz + P_{atm}$ where ρ_w is the density of water, g
738 is the acceleration due to gravity and atmospheric pressure P_{atm} is set to 0.1
739 MPa. The yield stress (15) is thus linearly increasing with depth, see Figure
740 6b. We assume the pore-pressure in the fault is higher than in the surround-
741 ing rock so that although the effective stresses off the fault are depth-variable,
742 effective normal stress on the fault is constant below some depth, see Fig-
743 ure 6b (*Rice, 1992*). Fixing the internal friction parameter ϕ sets the slope
744 of the yield stress and the yield stress at Earth's surface can be increased
745 or decreased by changing the value of the cohesion c , which we assume is
746 constant with depth. We vary cohesion between 40 and 50 MPa, which are
747 reasonable depth-averaged values of those derived from Hoek-Brown param-
748 eters for many rock strength models (*Roten et al., 2016*). The parameters
749 we use in our simulations are given in Table 5.

750 To determine grid spacing for our application simulations, *Ranjith (2008)*

Table 5: Parameters used in application simulations.

Parameter	Definition	Value
L_z	fault length	24 km
L_y	off-fault domain length	24 km
μ	shear modulus	36 GPa
ρ	density	2800 kg/m ³
c_s	shear wave speed	3.586 km/s
ρ_w	density of water	1000 kg/m ³
σ_n	normal stress on fault	depth-variable
τ^∞	remote shear stress	10 ⁻⁷ MPa
a	rate-and-state parameter	depth-variable
b	rate-and-state parameter	depth-variable
D_c	critical slip distance	8 mm
V_p	plate rate	10 ⁻⁹ m/s
V_0	reference velocity	10 ⁻⁶ m/s
f_0	reference friction coefficient	0.6
c	cohesion	variable
h	hardening modulus	variable
ϕ	internal friction angle	arctan(0.6)

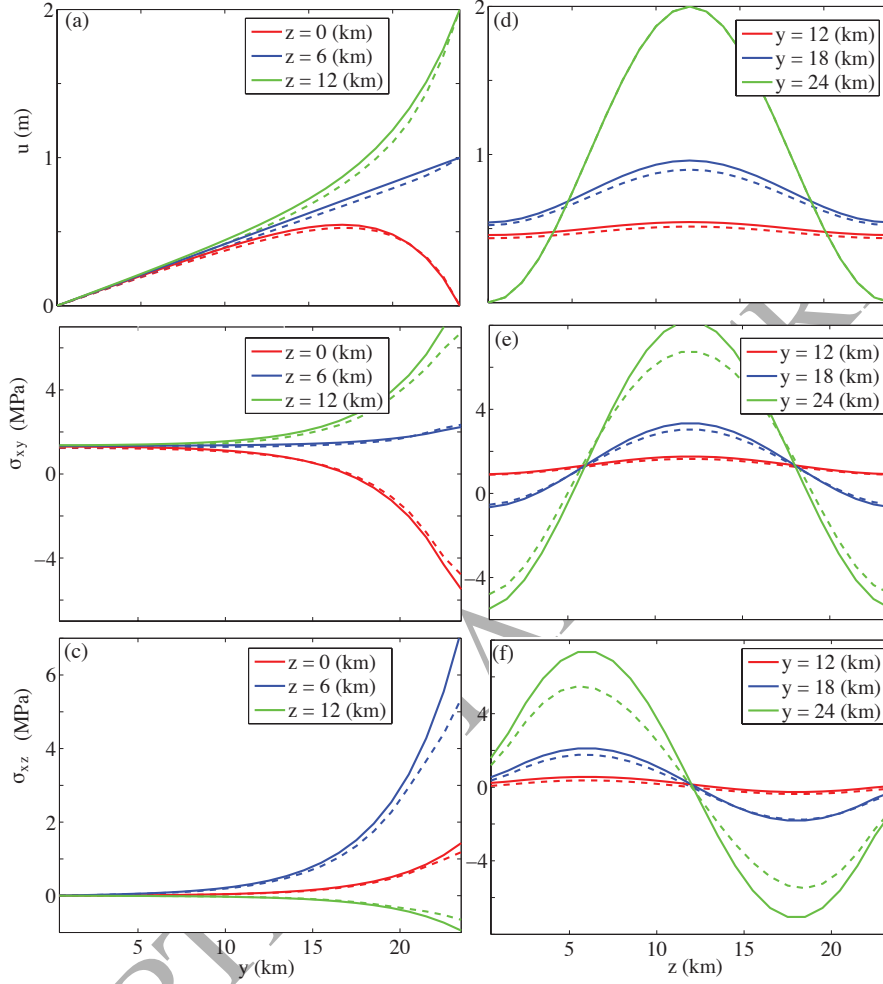


Figure 3: Contours of solution to (1) with boundary conditions (96) for elastic (solid lines) and plastic (dashed lines) material response. (a)-(b) displacement and (c)-(f) stress components. Plastic effects are seen most prominently in the stress contours which are reduced due to the yield condition.

751 found that for antiplane sliding between two anisotropic elastic materials,
 752 instability occurs for wave numbers below the critical wave number

753

$$k_{cr} = \frac{2(b-a)\sigma_n}{D_c \mu^*}, \quad (97)$$

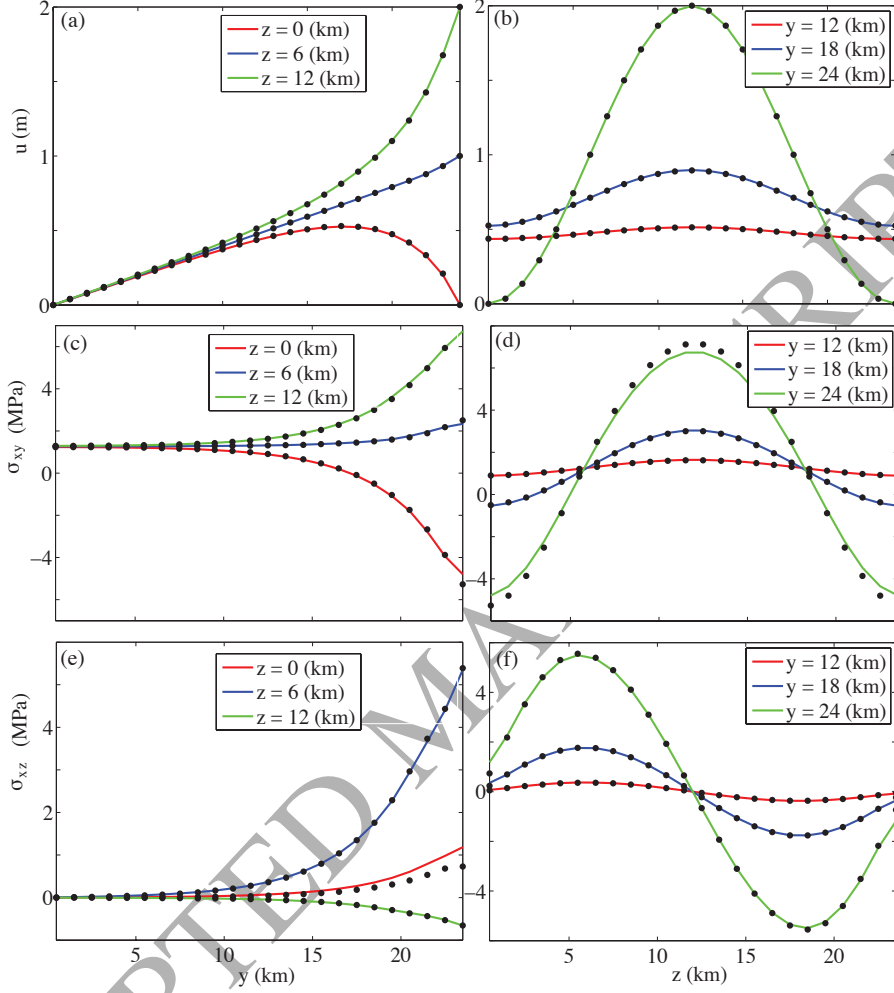


Figure 4: Contours of solution to (1) with boundary conditions (96) for plastic material response using the finite difference method (solid lines) and the finite element solution (black dots). (a)-(b) displacement and (c)-(f) stress components, with $N_y = N_z = 24$ points.

754 where

$$755 \mu^* = \sqrt{\det(\bar{C}^{ep})}. \quad (98)$$

756 Thus the length scale

$$757 h^* = \frac{2\pi}{k_{cr}} = \frac{\pi D_c \mu^*}{(b-a)\sigma_n} \quad (99)$$

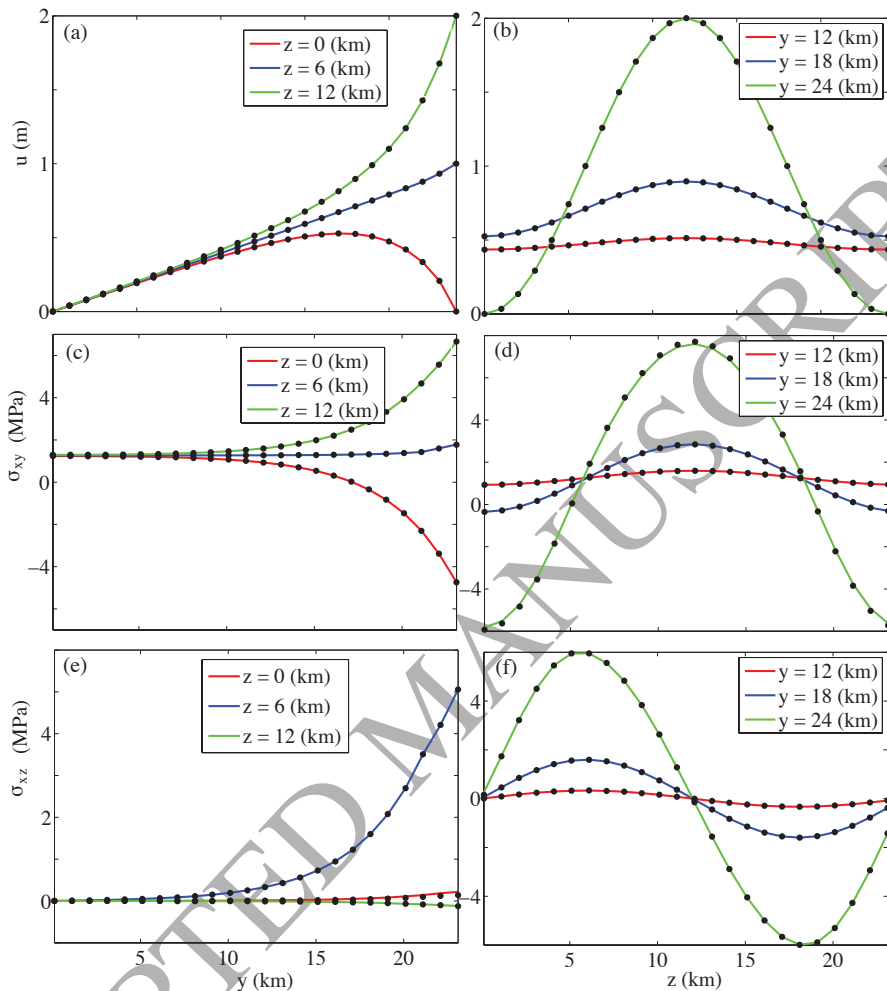


Figure 5: Contours of solution to (1) with boundary conditions (96) for plastic material response using the finite difference method (solid lines) and the finite element solution (black dots). (a)-(b) displacement and (c)-(f) stress components, with $N_y = N_z = 120$ points.

758 must be resolved by the grid to ensure accuracy of the solution.

759 As in *Erickson and Dunham* (2014), we also need to resolve the region
 760 of rapid strength degradation immediately behind the tip of a propagating
 761 rupture, which is typically much smaller than h^* , and involves the rate-
 762 and-state parameters a and b in a different manner. By analogy to the

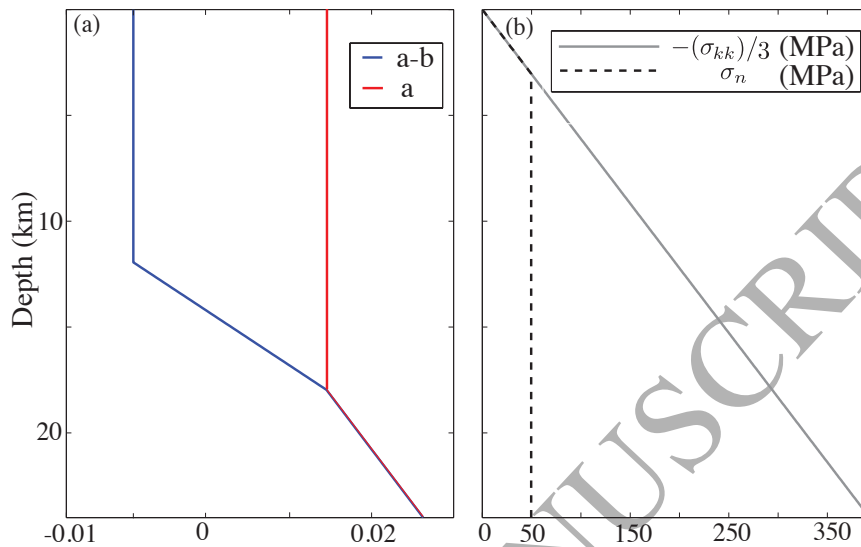


Figure 6: (a) Frictional parameters $a - b$ vary with depth. (b) Normal stress σ_n on fault vs. normal stresses in medium.

763 corresponding elastic problem (Ampuero and Rubin, 2008), we anticipate
 764 that this length scale will be approximately

$$765 \quad L_b = \frac{\mu^* D_c}{b \sigma_n}. \quad (100)$$

766 For all of our simulations, events nucleate near the transition zone from
 767 velocity weakening to velocity strengthening (at a depth of approximately 10
 768 km) and we chose values for parameters η and h primarily for computational
 769 (grid resolution) purposes. Since we use a variable grid spacing, we resolve
 770 h^* and L_b in our simulations with at least 60 and 5 grid points (respectively)
 771 near the free surface, with fewer (down to 12 and 1 grid point, respectively)
 772 at the nucleation depth, which we note seems less than desirable. To test that
 773 this grid spacing is adequate, however, we double the number of grid points
 774 for one scenario and the results appear qualitatively similar, see Appendix C.
 775 For the viscoplastic simulations we resolve the viscous relaxation time scale
 776 η/μ with at least 5 time steps.

777 For some parameter regimes, plastic yielding during the interseismic pe-
 778 riod is possible. For example, a decrease in cohesion c decreases the size of the
 779 elastic domain, so that plastic yielding can occur at lower stress states, see

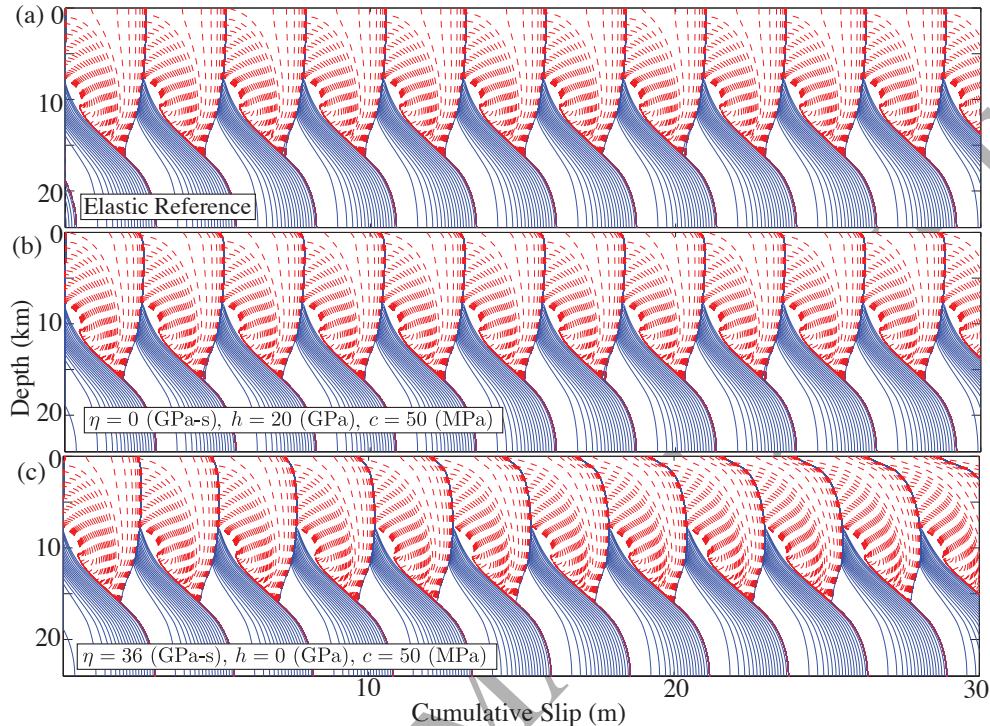


Figure 7: Snapshots of cumulative slip profiles plotted at 5-s intervals during interseismic period when $\max(V) \leq 1$ mm/s and dashed red profiles plotted at 1 s intervals during quasi-dynamic rupture for (a) elastic reference case, (b) $\eta = 0$ GPa-s, $h = 20$ GPa, $c = 50$ MPa, and (c) $\eta = 36$ GPa-s, $h = 0$ GPa, $c = 50$ MPa.

780 Figure 2. Although in reality plastic yielding may occur during all phases of
 781 the earthquake cycle, we chose to explore scenarios where plastic response is
 782 limited to the coseismic phase. This choice was made because viscoplasticity
 783 introduces the time scale η/h which must be resolved by the time-stepping
 784 method. For small values of η/h , the effective response during rupture is
 785 plastic. Unfortunately, small η/h cannot be resolved during the interseis-
 786 mic phase without taking unreasonably small time steps, thus we considered
 787 large values of c such that plastic response occurs only at those stress levels
 788 attained during rupture. The study of plastic yielding during all phases of
 789 the earthquake cycle are deferred to future work.

790 Figures 7 and 8 show cumulative slip profiles plotted at 5-s intervals
 791 during the interseismic period, which we define to be when $\max(V) \leq 1$

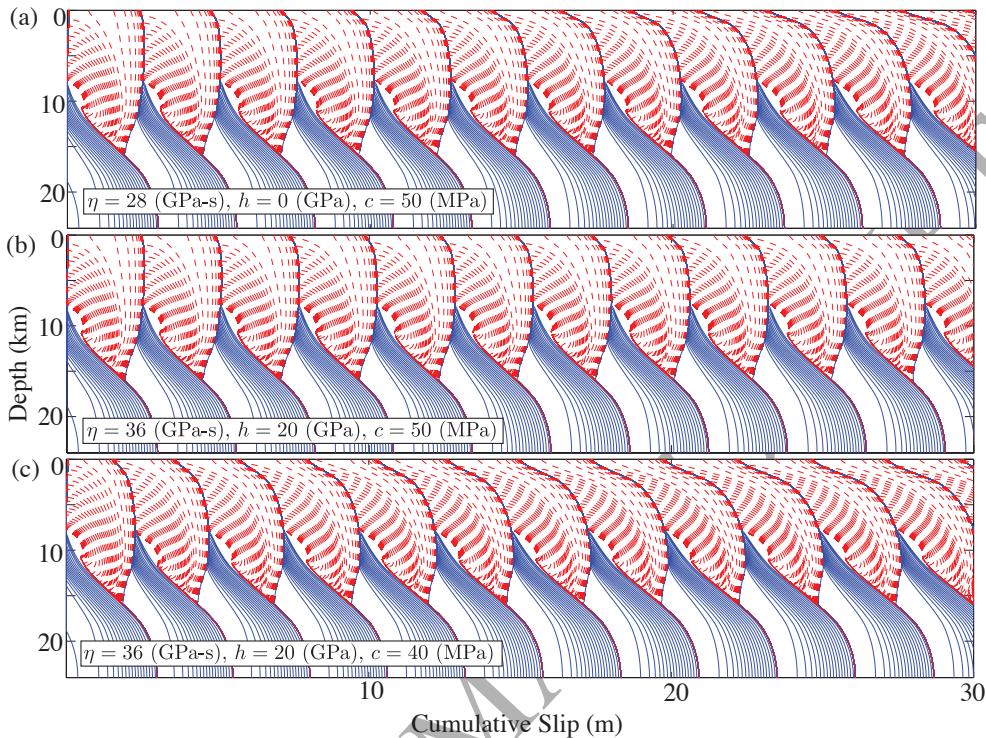


Figure 8: Snapshots of cumulative slip profiles plotted at 5-a intervals during interseismic period when $\max(V) \leq 1$ mm/s and dashed red profiles plotted at 1 s intervals during quasi-dynamic rupture for (a) $\eta = 28$ GPa-s, $h = 0$ GPa, $c = 50$ MPa, (b) $\eta = 36$ GPa-s, $h = 20$ GPa, $c = 50$ MPa, and (c) $\eta = 36$ GPa-s, $h = 20$ GPa, $c = 40$ MPa.

792 mm/s, and in dashed red contours every 1 s during quasi-dynamic rupture.
 793 Figure 7(a) is the elastic reference case used in *Erickson and Dunham* (2014),
 794 where periodic cycles emerge. Slip below the velocity-weakening region creeps
 795 interseismically and approximately 3 m of slip occurs at the surface during
 796 each event. Note that during each event, the upper section of the fault
 797 catches up with slip at depth, characteristic of an elastic material response.
 798 For the plastic simulations, in all cases we found that after the first rupture,
 799 slip in the shallow surface is less than the slip at depth. The evolution of this
 800 slip deficit with each subsequent event is dictated by the plasticity model,
 801 however.

802 Figure 7(b) shows results from considering rate-independent plasticity
 803 with hardening parameter $h = 20$ GPa and cohesion $c = 50$ MPa. Plastic

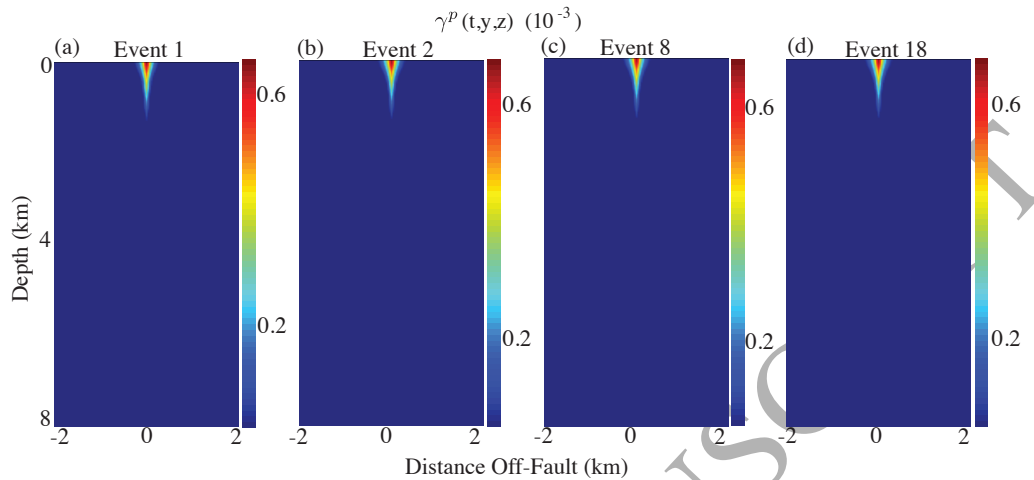


Figure 9: Off-fault equivalent plastic strain for $\eta = 0$ GPa-s, $h = 20$ GPa, $c = 50$ MPa after the first, second, eighth and eighteenth rupture events. The magnitude and off-fault extent (~ 100 m during first rupture only) of plastic strain effectively saturates after the first event.

804 response occurs during the first event when the rupture reaches approxi-
 805 mately 3 km depth, but has only a slight influence on slip above this depth.
 806 During the first rupture, a small slip deficit emerges above ~ 1 km depth.
 807 Because hardening causes the yield surface to expand, the response during
 808 subsequent events is effectively elastic and the slip deficit remains largely un-
 809 changed. Figure 7(c) shows results from a viscoplastic simulation (without
 810 hardening) with $\eta = 36$ GPa-s and $c = 50$ MPa. The slip deficit in the upper
 811 3 km increases with subsequent ruptures, and after the tenth event, the slip
 812 deficit at the surface is approximately 2 m.

813 To assess the sensitivity to viscosity, we decrease η from 36 to 28 GPa-s,
 814 seen in Figure 8(a). The slip deficit in the upper 3 km also increases with
 815 subsequent rupture, and after the 10th event the slip deficit at the surface is
 816 approximately 3 m, suggesting that the slip deficit will increase at a faster
 817 rate for lower values of η for the viscoplastic model without hardening. Figure
 818 8(b) shows results from combined viscoplastic and hardening effects. For
 819 $\eta = 36$ GPa-s, $h = 20$ GPa and $c = 50$ MPa, the slip deficit increases with
 820 each rupture, but at a decreasing rate, and reaches a limiting value of ~ 1 m.

821 Decreasing the cohesion to 40 MPa, as shown in Figure 8(c), gener-
 822 ates a larger slip deficit (approximately 3.5 m at the surface after the 10th

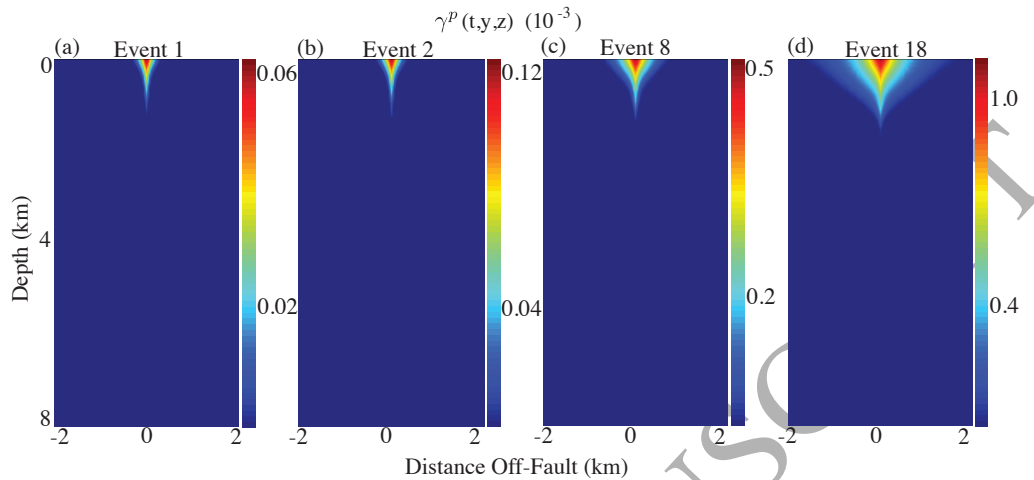


Figure 10: Off-fault equivalent plastic strain for $\eta = 36$ GPa-s, $h = 0$ GPa, $c = 50$ MPa after the first, second, eighth and eighteenth rupture events. The magnitude and off-fault extent (additional ~ 100 m per rupture) of plastic strain increases at an approximately constant rate with each rupture during the first 18 events.

823 event) than the analogous simulation in Figure 8(b), although with hardening
 824 present this deficit also saturates after several ruptures.

825 For the values we considered, cohesion determines the depth at which
 826 plastic response occurs during rupture (confined to about 1-2 km below
 827 Earth's surface). Figure 9 illustrates the evolution in off-fault equivalent
 828 plastic strain for the rate-independent simulation from Figure 7(a), during
 829 the first, second, eighth and eighteenth events. The first event generates
 830 plastic strain at depths above ~ 1 km and off the fault to about 200 m at the
 831 surface. The maximum value at the fault surface is approximately 0.7 mil-
 832 listrain and little increase in either extent or magnitude occurs after the first
 833 event. Figure 10 is the analogous figure for the viscoplastic model without
 834 hardening from Figure 7(b). The first event generates a maximum value of
 835 0.06 millistrain at the fault surface, extending out to approximately 300 m
 836 and to a depth of ~ 1 km. During all subsequent events the maximum value
 837 of plastic strain increases.

838 Adding hardening to the viscoplastic model decreases the magnitude and
 839 extent of additional plastic strain with each rupture, see Figure 11, so that
 840 by the eighteenth rupture, the distribution remains relatively unchanged by
 841 subsequent events. Figure 12 illustrates the effect of a decrease in cohesion

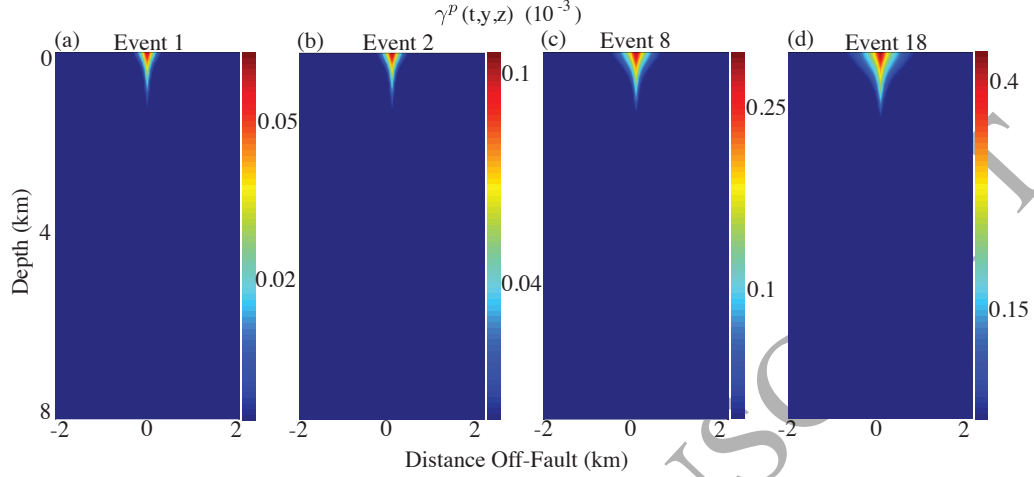


Figure 11: Off-fault equivalent plastic strain for $\eta = 36$ GPa-s, $h = 20$ GPa, $c = 50$ MPa after the first, second, eight and eighteenth rupture events. The magnitude and off-fault extent (~ 100 m during first rupture only) of plastic strain increases at an approximately decreasing rate with each rupture. After 18 events, the extent has saturated at < 1 km at the surface.

842 (from 50 to 40 MPa) which effectively lowers the yield stress so that plastic
 843 straining occurs at lower depths compared to previous simulations. Com-
 844 pared to the results shown in Figure 11, a decrease in cohesion increases the
 845 depth of plastic strain from 1 to 2 km during the first event. In addition, a
 846 decrease in cohesion generates more plastic strain and with greater extent.
 847 By the eighteenth event, plastic strain extends beyond 2 km at the surface.

848 The amount of tectonic offset accommodated by plastic strain, $u^p(t, z)$,
 849 can be computed by integrating the off-fault plastic strain, namely

$$850 \quad u^p(t, z) = 2 \int_0^{L_y} \gamma_{xy}^p(t, y, z) dy. \quad (101)$$

851 At the surface $z = 0$, the time history of u^p is plotted in Figure 13 and illus-
 852 trates how much tectonic offset is accommodated by inelastic deformation for
 853 different plasticity models. In particular, when rate-independent plasticity
 854 with hardening is used (cyan), the amount of offset due to inelastic deforma-
 855 tion is about 0.2 m after the first event and increases almost negligibly after
 856 the first event. If a viscoplastic relaxation is added (green), however, the
 857 amount of offset is lower during the first event, but increases with each rup-
 858 ture, reaching approximately 0.2 m after ~ 10 events. An increasing amount

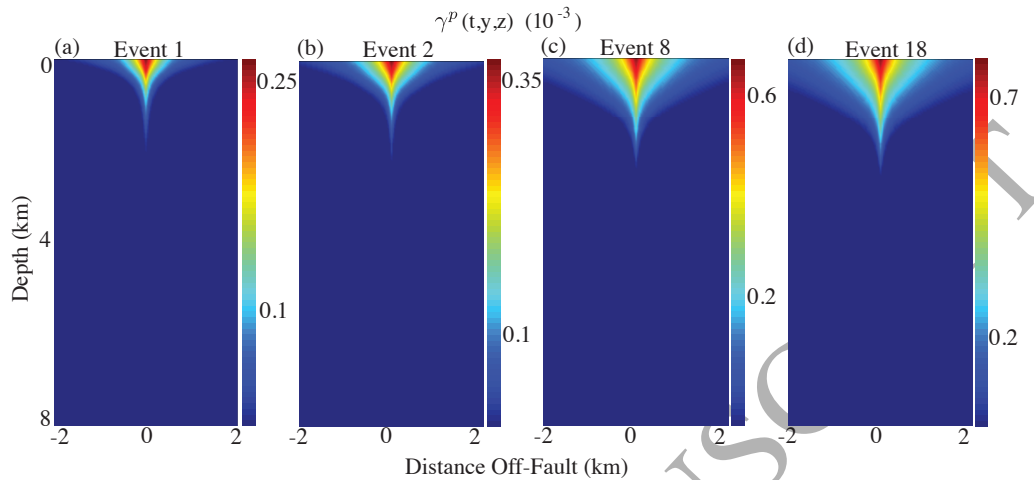


Figure 12: Off-fault equivalent plastic strain for $\eta = 36$ GPa-s, $h = 20$ GPa, $c = 40$ MPa after the first, second, eight and eighteenth rupture events. The magnitude and off-fault extent (~ 1 km during first rupture only) of plastic strain increases at an approximately decreasing rate with each rupture. After 18 events, the extent has begun to saturate near 2 km.

859 of offset accommodated by inelastic deformation occurs with each rupture
 860 for the viscoplastic models without hardening (black, blue, red), with lower
 861 values of viscosity generating greater amounts of inelastic deformation. For
 862 $\eta = 20$ GPa-s, for example, approximately 2 m of tectonic off-set is accommo-
 863 dated by inelastic strain after ~ 10 events. The rate-independent simulation
 864 with hardening present (cyan) reveals that an upper limit to the amount of
 865 inelastic deformation exists, by virtue of the fact that hardening causes in
 866 expansion of the yield surface, as illustrated in Figure 2. The viscoplastic
 867 simulations with hardening (green and purple) show that inelastic yielding
 868 continues to occur (with greater overall amounts for lower values in cohesion),
 869 but at a decreasing rate, i.e for decreasing du^p/dt . Only the viscoplastic sim-
 870 ulations without hardening (black, blue, red) reveal that inelastic yielding
 871 continues to occur with an increasing amount of plastic strain accruing with
 872 each event ($du^p/dt \geq 0$).

873 10. Discussion

874 We have developed a finite difference method to account for off-fault
 875 plastic response over many quasi-dynamic ruptures. The computational

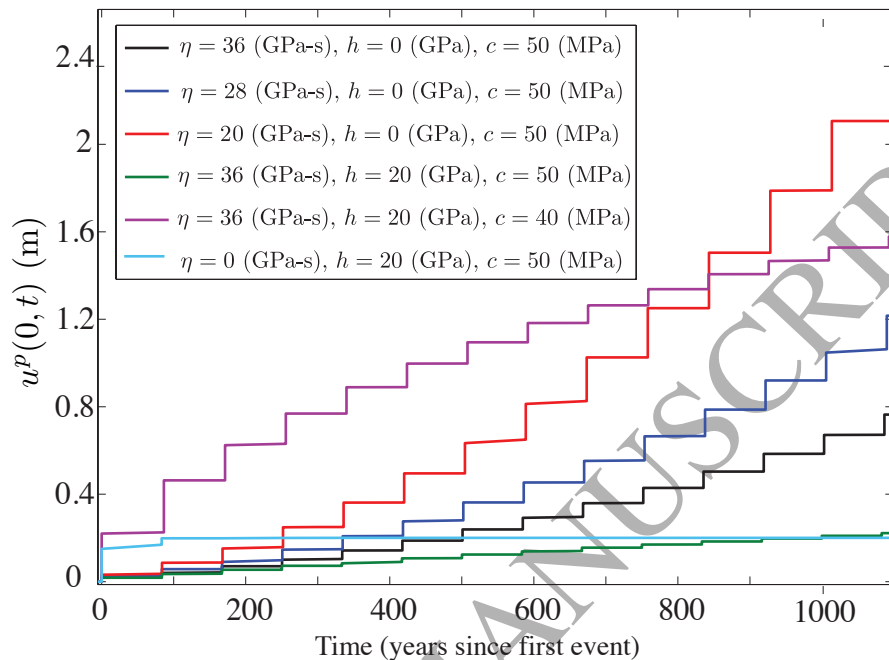


Figure 13: Time history of integrated plastic strain at the surface showing amount of tectonic offset accommodated by inelastic deformation.

876 framework can model both rate-independent plasticity and viscoplasticity, al-
 877 though we found that isotropic hardening is necessary in the rate-independent
 878 model for solveability of the underlying equations. We considered a Drucker-
 879 Prager model (which reduces to von-Mises plasticity in the antiplane scenario
 880 we considered) with a depth-dependent yield stress. Numerical results were
 881 verified through convergence tests and comparisons with the solution from a
 882 finite element software package. Future work includes a deeper exploration
 883 of parameter space. For example, the inclusion of a depth dependency of
 884 the internal friction angle and cohesion (like those derived in *Roten et al.*
 885 (2016)) will be considered. The effects of hardening and viscosity will fur-
 886 ther be explored, as our choices for these parameters were chosen primarily
 887 for efficiency of computation.

888 For the parameter study in this work, we found that viscosity, hardening,
 889 and cohesion all influence the extent and magnitude of off-fault plastic strain
 890 and all scenarios give rise to a shallow slip deficit. The inclusion of hard-

891 ening in all models sets an upper limit on the slip deficit, which is reached
 892 at a faster rate for lower values of viscosity. The viscoplastic models with
 893 no hardening, however, give rise to the largest slip deficits which increase
 894 continuously with subsequent rupture. Our results suggest that cumulative
 895 inelastic deformation over the course of many events can account for a sig-
 896 nificant amount of tectonic offset. We found that per rupture, ~ 0.1 m of
 897 integrated plastic strain accrues, corresponding to $\sim 10\%$ of the tectonic de-
 898 formation budget. Results from our model compare well to the observations
 899 of *Meade et al.* (2013) who estimate that $6\% \pm 9\%$ of deformation occurs off
 900 of several major strike-slip faults.

901 11. Acknowledgments

902 We thank the editor at JMPS for handling this manuscript, as well as
 903 four anonymous reviewers for helpful comments. This work was initiated
 904 while B.A.E. was supported by the NSF under Award No. EAR-0948304
 905 and completed with support from NSF under Award No. EAR-1547603 and
 906 by the Southern California Earthquake Center. SCEC is funded by NSF
 907 Cooperative Agreement EAR-0529922 and USGS Cooperative Agreement
 908 07HQAG0008 (SCEC contribution number 7166).

909 Appendix A. The Coordinate Transform and Penalty Parameters

910 As stated in section 6, we desire finer grid resolution in the domain near
 911 the fault and close to the free surface $z = 0$. Using coordinate transforms,
 912 we map the (y, z) grid in $[0, L_y] \times [0, L_z]$ with unequally spaced nodes, to a
 913 computational domain $(\xi_1, \xi_2) \in [0, 1] \times [0, 1]$ with equal grid spacings $(N_{\xi_1} + 1$
 914 and $N_{\xi_2} + 1$ grid points in each direction, with $\Delta\xi_1 = 1/N_{\xi_1}$, $\Delta\xi_2 = 1/N_{\xi_2}$.
 915 We let $N = (N_{\xi_1} + 1)(N_{\xi_2} + 1)$. The mapping is given by

$$916 \quad y = l_Y \tan(\tan^{-1}(L_y/l_Y)\xi_1) \quad (\text{A.1a})$$

$$917 \quad z = l_Z \tan(\tan^{-1}(L_z/l_Z)\xi_2). \quad (\text{A.1b})$$

918 Parameters $l_Y, l_Z > 0$ control the strength to which nodes are clustered
 919 near the fault and surface (respectively). The mapping (A.1) is invertible,
 920 with $\frac{\partial y}{\partial \xi_1}, \frac{\partial z}{\partial \xi_2} > 0$. The Jacobian J of the transformation is

$$921 \quad J = \begin{bmatrix} \frac{\partial y}{\partial \xi_1} & 0 \\ 0 & \frac{\partial z}{\partial \xi_2} \end{bmatrix} \quad (\text{A.2})$$

922 with determinant $|\mathbf{J}| = \frac{\partial \mathbf{y}}{\partial \xi_1} \otimes \frac{\partial \mathbf{z}}{\partial \xi_2}$ where $\frac{\partial \mathbf{y}}{\partial \xi_1}$ denotes the diagonal coefficient
 923 matrix, and $\frac{\partial \mathbf{y}}{\partial \xi_1}^{-1}$ is its inverse (reciprocals along the diagonal). Using the
 924 notation introduced in section 6, the SBP-SAT discretization of (33) on the
 925 computational domain is given by

$$\mathbf{0} = \mathbf{D}_{2\xi_1}^{\mathbf{a}_{11}} \mathbf{du} + \mathbf{D}_{\xi_1} \mathbf{a}_{12} \mathbf{D}_{\xi_2} \mathbf{du} + \mathbf{D}_{\xi_2} \mathbf{a}_{21} \mathbf{D}_y \mathbf{du} + \mathbf{D}_{2\xi_2}^{\mathbf{a}_{22}} \mathbf{du} + \tilde{\mathbf{P}}_L + \tilde{\mathbf{P}}_R + \tilde{\mathbf{P}}_T + \tilde{\mathbf{P}}_B, \quad (\text{A.3})$$

926 where the SAT penalty vectors enforcing boundary conditions (41) are

$$\tilde{\mathbf{P}}_L = \mathbf{H}_{\xi_1}^{-1} (\boldsymbol{\alpha}_L + \beta \mathbf{H}_{\xi_2}^{-1} (-\mathbf{a}_{11} \mathbf{S}_{\xi_1} - \mathbf{a}_{12} \mathbf{D}_{\xi_2})^T) \mathbf{H}_{\xi_2} \mathbf{E}_0 (\mathbf{du}_L - \mathbf{dg}_L) \quad (\text{A.4a})$$

$$\tilde{\mathbf{P}}_R = \mathbf{H}_{\xi_1}^{-1} (\boldsymbol{\alpha}_R + \beta \mathbf{H}_{\xi_2}^{-1} (\mathbf{a}_{11} \mathbf{S}_{\xi_1} + \mathbf{a}_{12} \mathbf{D}_{\xi_2})^T) \mathbf{H}_{\xi_2} \mathbf{E}_N (\mathbf{du}_R - \mathbf{dg}_R) \quad (\text{A.4b})$$

$$\tilde{\mathbf{P}}_T = -\mathbf{H}_{\xi_2}^{-1} (\mathbf{I}_{\xi_1} \otimes \mathbf{E}_0) ([-\mathbf{a}_{22} \mathbf{S}_{\xi_2} \mathbf{du} - \mathbf{a}_{21} \mathbf{D}_{\xi_1} \mathbf{du}]_T - \tilde{\mathbf{d}}\mathbf{g}_T) \quad (\text{A.4c})$$

$$\tilde{\mathbf{P}}_B = -\mathbf{H}_{\xi_2}^{-1} (\mathbf{I}_{\xi_1} \otimes \mathbf{E}_N) ([\mathbf{a}_{22} \mathbf{S}_{\xi_2} \mathbf{du} + \mathbf{a}_{21} \mathbf{D}_{\xi_1} \mathbf{du}]_B - \tilde{\mathbf{d}}\mathbf{g}_B) \quad (\text{A.4d})$$

932 where the modified boundary data are

$$\tilde{\mathbf{d}}\mathbf{g}_T = \frac{\partial \mathbf{y}}{\partial \xi_1} \mathbf{d}\mathbf{g}_T \quad (\text{A.5a})$$

$$\tilde{\mathbf{d}}\mathbf{g}_B = \frac{\partial \mathbf{y}}{\partial \xi_1} \mathbf{d}\mathbf{g}_B. \quad (\text{A.5b})$$

935 The modified diagonal coefficient matrices in (A.4) are

$$\mathbf{a}_{11} = \mathbf{C}_{11}^{ep} \left(\frac{\partial \mathbf{y}}{\partial \xi_1}^{-1} \otimes \frac{\partial \mathbf{z}}{\partial \xi_2} \right) \quad (\text{A.6a})$$

$$\mathbf{a}_{12} = \mathbf{C}_{12}^{ep} \quad (\text{A.6b})$$

$$\mathbf{a}_{21} = \mathbf{C}_{21}^{ep} \quad (\text{A.6c})$$

$$\mathbf{a}_{22} = \mathbf{C}_{22}^{ep} \left(\frac{\partial \mathbf{y}}{\partial \xi_1} \otimes \frac{\partial \mathbf{z}}{\partial \xi_2}^{-1} \right) \quad (\text{A.6d})$$

940 correspond to the moduli

$$a_{11} = C_{11}^{ep} \frac{\partial \xi_1}{\partial y} \quad (\text{A.7a})$$

$$a_{12} = C_{12}^{ep} \quad (\text{A.7b})$$

$$a_{21} = C_{21}^{ep} \quad (\text{A.7c})$$

$$a_{22} = C_{22}^{ep} \frac{\partial \xi_2}{\partial z} \quad (\text{A.7d})$$

945 of the transformed (continuous) problem, and we use the notation $a_{11,i,j} =$
 946 $a_{11}(y_j, z_i)$ as in section 6. Letting

$$\bar{\mathbf{A}} = \begin{bmatrix} \mathbf{a}_{11} & \mathbf{a}_{12} \\ \mathbf{a}_{21} & \mathbf{a}_{22} \end{bmatrix}, \quad (\text{A.8})$$

948 symmetry of $\bar{\mathbf{A}}$ follows that of the 2×2 matrix \bar{C}^{ep} given by (34). That $\bar{\mathbf{A}}$
949 is positive-definite also follows from \bar{C}^{ep} : Express $\bar{\mathbf{A}}$ via the Schur decompo-
950 sition $\bar{\mathbf{A}} = \mathbf{X}^T \mathbf{S} \mathbf{X}$, where

$$\mathbf{S} = \begin{bmatrix} \mathbf{a}_{11} & \mathbf{0} \\ \mathbf{0} & \mathbf{a}_{22} - \mathbf{a}_{21} \mathbf{a}_{11}^{-1} \mathbf{a}_{12} \end{bmatrix} \quad (\text{A.9})$$

952 and

$$\mathbf{X} = \begin{bmatrix} \mathbf{I} & \mathbf{a}_{11}^{-1} \mathbf{a}_{12} \\ \mathbf{0} & \mathbf{I} \end{bmatrix}. \quad (\text{A.10})$$

954 Since \mathbf{S} is a diagonal matrix, its eigenvalues lie along the diagonal. Positive-
955 definiteness of \bar{C}^{ep} guarantees that each element along the diagonal of \mathbf{C}_{11}^{ep}
956 is positive and the transformation (A.1) maintains that the diagonal matrix
957 \mathbf{a}_{11} has positive elements. The diagonal matrix $\mathbf{a}_{22} - \mathbf{a}_{21} \mathbf{a}_{11}^{-1} \mathbf{a}_{12} = (\frac{\partial \mathbf{y}}{\partial \xi_1} \otimes$
958 $\frac{\partial \mathbf{z}}{\partial \xi_2}^{-1}) [\mathbf{C}_{11}^{ep}]^{-1} (\mathbf{C}_{11}^{ep} \mathbf{C}_{22}^{ep} - \mathbf{C}_{12}^{ep} \mathbf{C}_{21}^{ep})$ has positive elements by construction of the
959 mapping and positive-definiteness of \bar{C}^{ep} . Thus positive-definiteness of $\bar{\mathbf{A}}$
960 follows from that of \mathbf{S} by the Sylvester Law of Inertia (*Golub and Van Loan*,
961 2013).

962 Applying the energy method to (A.3) and a proper choice of penalty
963 parameters (given shortly) yields $\frac{d}{dt} \mathbf{dE} \leq 0$, where

$$\mathbf{dE} = \frac{1}{2} \mathbf{dU}^T (\mathbf{H}_{\xi_1} \otimes \mathbf{H}_{\xi_2}) \bar{\mathbf{A}} \mathbf{dU} + \frac{1}{2} \mathbf{du}^T (\mathbf{R}_{\xi_1}^{\mathbf{a}_{11}} \otimes \mathbf{H}_{\xi_2}) \mathbf{du} + \frac{1}{2} \mathbf{du}^T (\mathbf{H}_{\xi_1} \otimes \mathbf{R}_{\xi_2}^{\mathbf{a}_{22}}) \mathbf{du} + U_1 + U_2, \quad (\text{A.11})$$

964 where $\mathbf{dU} = [\mathbf{D}_{\xi_1} \mathbf{du} \ \mathbf{D}_{\xi_2} \mathbf{du}]^T$. U_1 and U_2 are non-negative quantities that
965 that arise from the weak enforcement of Dirichlet conditions, detailed shortly.

967 Note that uniform grid spacing, as considered in section 6, is the special
968 case $\ell_Y, \ell_Z \rightarrow \infty$ and the transformation merely scales the overall size of the
969 domain. In the case of uniform grid spacing, $\bar{\mathbf{A}} = \bar{C}^{ep}$. The stability results
970 of section 6 are thus a special case of the results here.

971 The penalty parameters in (A.4) are derived in *Virta and Mattsson* (2014)
972 and given here. The $N \times N$ diagonal coefficient matrix \mathbf{a}_{11} has j, k^{th} entry
973 $\mathbf{a}_{11,j,k}$. *Virta and Mattsson* (2014) find that penalty parameter $\beta = -1$,

974 and penalty (diagonal) matrices $\boldsymbol{\alpha}_L$, $\boldsymbol{\alpha}_R$ have components obtained by first
 975 defining diagonal matrices \mathbf{b}_{1L} , \mathbf{b}_{1R} , \mathbf{b}_{2L} and \mathbf{b}_{2R} which have components

$$976 \quad b_{1Lj,j} = \beta_p(\Delta\xi_1)\lambda_{Lj}/(a_{11j,1})^2 \quad (\text{A.12a})$$

$$977 \quad b_{1Rj,j} = \beta_p(\Delta\xi_1)\lambda_{Rj}/(a_{11j,N_{\xi_1}})^2 \quad (\text{A.12b})$$

$$978 \quad b_{2Lj,j} = \delta_p(\Delta\xi_1)\lambda_{j,1}/(a_{22j,1})^2 \quad (\text{A.12c})$$

$$979 \quad b_{2Rj,j} = \delta_p(\Delta\xi_1)\lambda_{j,N_{\xi_1}}/(a_{22j,N_{\xi_1}})^2 \quad (\text{A.12d})$$

980 along the diagonal, where $\beta_p = 36/99$ and $\delta_p = 1/2$ (for the second order
 981 operators we consider),

$$982 \quad \lambda_{Lj} = \min(\lambda_{j,0}, \lambda_{j,1}), j = 0, \dots, N_{\xi_2} \quad (\text{A.13a})$$

$$983 \quad \lambda_{Rj} = \min(\lambda_{j,N_{\xi_1}-1}, \lambda_{j,N_{\xi_1}}), j = 0, \dots, N_{\xi_2}, \quad (\text{A.13b})$$

984 and

$$985 \quad \lambda_{j,k} = \frac{1}{2} \left(a_{11j,k} + a_{22j,k} - \sqrt{(a_{11j,k} - a_{22j,k})^2 + 4(a_{12j,k})^2} \right). \quad (\text{A.14a})$$

986 The positive quantities given in the incremental internal energy are

$$987 \quad U_1 = \mathbf{U}_L^T \mathbf{H}_3 \mathbf{T}_L \mathbf{U}_L \quad (\text{A.15a})$$

$$988 \quad U_2 = \mathbf{U}_R^T \mathbf{H}_3 \mathbf{T}_R \mathbf{U}_R \quad (\text{A.15b})$$

989 for vectors

$$990 \quad \mathbf{U}_L = [\mathbf{du}_L^T \quad (\mathbf{B}^{\mathbf{a}_{11}} \mathbf{S}_{\xi_1} \mathbf{du})_L^T \quad (\mathbf{a}_{12} \mathbf{D}_{\xi_1} \mathbf{du})_L^T]^T, \quad (\text{A.16a})$$

$$991 \quad \mathbf{U}_R = [\mathbf{du}_R^T \quad (\mathbf{B}^{\mathbf{a}_{11}} \mathbf{S}_{\xi_1} \mathbf{du})_R^T \quad (\mathbf{a}_{12} \mathbf{D}_{\xi_1} \mathbf{du})_R^T]^T, \quad (\text{A.16b})$$

$$992 \quad \mathbf{H}_3 = \text{diag}([\mathbf{H}_{\xi_1} \otimes \mathbf{H}_{\xi_2}, \quad \mathbf{H}_{\xi_1} \otimes \mathbf{H}_{\xi_2}, \quad \mathbf{H}_{\xi_1} \otimes \mathbf{H}_{\xi_2}]). \quad (\text{A.16c})$$

993 Matrix $\mathbf{B}^{\mathbf{a}_{11}}$ is a coefficient matrix for \mathbf{a}_{11} formed in a special way (see *Virta*
 994 *and Mattsson* (2014) for details). Matrices

$$995 \quad \mathbf{T}_L = \begin{bmatrix} -\boldsymbol{\alpha}_L & -\mathbf{1} & -\mathbf{1} \\ -\mathbf{1} & \mathbf{b}_{1R} & \mathbf{0} \\ -\mathbf{1} & \mathbf{0} & \mathbf{b}_{2R} \end{bmatrix} \quad (\text{A.17a})$$

996 and

$$997 \quad \mathbf{T}_R = \begin{bmatrix} -\boldsymbol{\alpha}_R & -\mathbf{1} & -\mathbf{1} \\ -\mathbf{1} & \mathbf{b}_{1L} & \mathbf{0} \\ -\mathbf{1} & \mathbf{0} & \mathbf{b}_{2L} \end{bmatrix} \quad (\text{A.18a})$$

998 are shown to be positive semi-definite if

$$999 \quad \alpha_{L_j,j} \leq -\frac{1}{b_{1R_j,j}} - \frac{1}{b_{2R_j,j}}, \quad j = 0, \dots, N_{\xi_2} \quad (\text{A.19a})$$

$$1000 \quad \alpha_{R_j,j} \leq -\frac{1}{b_{1R_j,j}} - \frac{1}{b_{2R_j,j}}, \quad j = 0, \dots, N_{\xi_2} \quad (\text{A.19b})$$

1001 (*Virta and Mattsson, 2014*).

1002 Appendix B. The Consistent Tangent Moduli

1003 The consistent tangent moduli for both rate-independent and viscoplas-
1004 ticity are derived here simultaneously. Applying a backward-Euler discretiza-
1005 tion to the flow rule (19), we have

$$1006 \quad \sigma_{ij}^{n+1} = C_{ijkl}(\epsilon_{kl}^{n+1} - \epsilon_{kl}^{p,n+1}) = C_{ijkl}(\epsilon_{kl}^{n+1} - \epsilon_{kl}^{p,n} - d\lambda^{n+1} \frac{s_{kl}^{n+1}}{2\bar{\tau}^{n+1}}). \quad (\text{B.1})$$

1007 The consistent elastoplastic tangent stiffness tensor $\mathcal{C}_{ijkl}^{ep,n+1} = \frac{\partial \sigma_{ij}^{n+1}}{\partial \epsilon_{kl}^{n+1}}$ can be
1008 computed by first defining a few terms. Following *Simo and Hughes* (1998),
1009 let $n_{ij} = s_{ij}/2\bar{\tau}$. Then

$$1010 \quad \frac{\partial n_{ij}}{\partial s_{kl}} = \frac{1}{\bar{\tau}} \left[\frac{1}{2} I_{ijkl} - n_{ij} n_{kl} \right], \quad (\text{B.2})$$

1011 where the fourth order, symmetric identity tensor

$$1012 \quad I_{ijkl} = \frac{1}{2} [\delta_{ik} \delta_{jl} + \delta_{il} \delta_{jk}]. \quad (\text{B.3})$$

1013 It is a quick exercise to show that

$$1014 \quad n_{ij}^{*,n+1} = n_{ij}^{n+1}, \quad (\text{B.4})$$

1015 and therefore we have

$$1016 \quad \frac{\partial \bar{\tau}^{*,n+1}}{\partial \epsilon_{kl}^{n+1}} = \frac{1}{\bar{\tau}^{*,n+1}} \sigma_{kl}^{*,n+1} \mu = 2\mu n_{kl}^{*,n+1} = 2\mu n_{kl}^{n+1}. \quad (\text{B.5})$$

1017 Next, recall the plastic consistency condition (71), which can be expressed

$$1018 \quad \bar{\tau}^{*,n+1} - \sigma_Y - h\gamma_p^n = (\eta/dt + \mu + h)d\lambda^{n+1} \quad (\text{B.6})$$

1019 where the rate-independent case is obtained by taking $\eta = 0$. Taking the
1020 partial derivative of (B.6) yields

$$1021 \quad \frac{\partial \bar{\tau}^{*,n+1}}{\partial \epsilon_{kl}^{n+1}} = (\eta/dt + \mu + h) \frac{\partial d\lambda^{n+1}}{\partial \epsilon_{kl}^{n+1}}. \quad (\text{B.7})$$

1022 Re-arranging (B.7) and substituting in (B.5) yields

$$1023 \quad \frac{\partial \Delta \lambda^{n+1}}{\partial \epsilon_{kl}^{n+1}} = \frac{2\mu}{\eta/dt + \mu + h} n_{kl}^{n+1}. \quad (\text{B.8})$$

1024 Also note that we have,

$$1025 \quad C_{ijmn} \frac{\partial s_{mn}}{\partial \epsilon_{kl}} = 2\mu \frac{\partial s_{ij}}{\partial \epsilon_{kl}}. \quad (\text{B.9})$$

1026 Therefore

$$1027 \quad \frac{\partial n_{ij}^{n+1}}{\partial \epsilon_{kl}^{n+1}} = \frac{\partial n_{ij}^{*,n+1}}{\partial \epsilon_{kl}^{n+1}} = \frac{\partial n_{ij}^{*,n+1}}{\partial \sigma_{mn}^{*,n+1}} \frac{\partial \sigma_{mn}^{*,n+1}}{\partial \epsilon_{kl}^{n+1}} = \frac{\partial n_{ij}^{*,n+1}}{\partial \sigma_{mn}^{*,n+1}} C_{mnkl} = 2\mu \frac{\partial n_{ij}^{*,n+1}}{\partial \sigma_{kl}^{*,n+1}} = 2\mu \frac{\partial n_{ij}^{n+1}}{\partial s_{kl}^{n+1}}. \quad (\text{B.10})$$

1028 When plastic straining is occurring (i.e. when $\lambda > 0$), we can compute the
1029 consistent elastoplastic tangent stiffness tensor by taking the partial deriva-
1030 tive of equation (B.1)

$$1031 \quad \mathcal{C}_{ijkl}^{ep,n+1} = \frac{\partial \sigma_{ij}^{n+1}}{\partial \epsilon_{ij}^{n+1}} = C_{ijkl} - \frac{\partial d\lambda^{n+1}}{\partial \epsilon_{kl}^{n+1}} \mu n_{ij}^{n+1} - d\lambda^{n+1} \mu \frac{\partial n_{ij}^{n+1}}{\partial \epsilon_{kl}^{n+1}} \quad (\text{B.11})$$

$$1032 \quad = C_{ijkl} - \frac{2\mu}{\eta/dt + \mu + h} n_{kl}^{n+1} 2\mu n_{ij}^{n+1} - d\lambda^{n+1} 2\mu \left(2\mu \frac{\partial n_{ij}^{n+1}}{\partial s_{kl}^{n+1}} \right) \quad (\text{B.12})$$

$$1033 \quad = C_{ijkl} - \frac{4\mu^2}{\eta/dt + \mu + h} n_{kl}^{n+1} n_{ij}^{n+1} - d\lambda^{n+1} 4\mu^2 \frac{1}{\bar{\tau}^{n+1}} \left[\frac{1}{2} I_{ijkl} - n_{ij}^{n+1} n_{kl}^{n+1} \right] \quad (\text{B.13})$$

1034 and the specific case for antiplane motion given in (73)-(75) for rate-independent
1035 plasticity, and (78)-(80) for viscoplasticity follow, using the notation $\mathcal{C}_{11}^{ep} =$
1036 \mathcal{C}_{xyxy}^{ep} , $\mathcal{C}_{22}^{ep} = \mathcal{C}_{xzxz}^{ep}$, $\mathcal{C}_{12}^{ep} = \mathcal{C}_{xyxz}^{ep}$, $\mathcal{C}_{21}^{ep} = \mathcal{C}_{xzyx}^{ep}$.

1037 Appendix C. Mesh Refinement

1038 We double the number of grid points used in the simulation shown in
1039 Figure 7(c) with $\eta = 36$, $h = 0$ and $c = 50$ MPa, see Fig. C.14. Although a
1040 bit more slip occurs with each rupture when mesh refining (note last event
1041 for each simulation, for example), the results appear qualitatively similar.

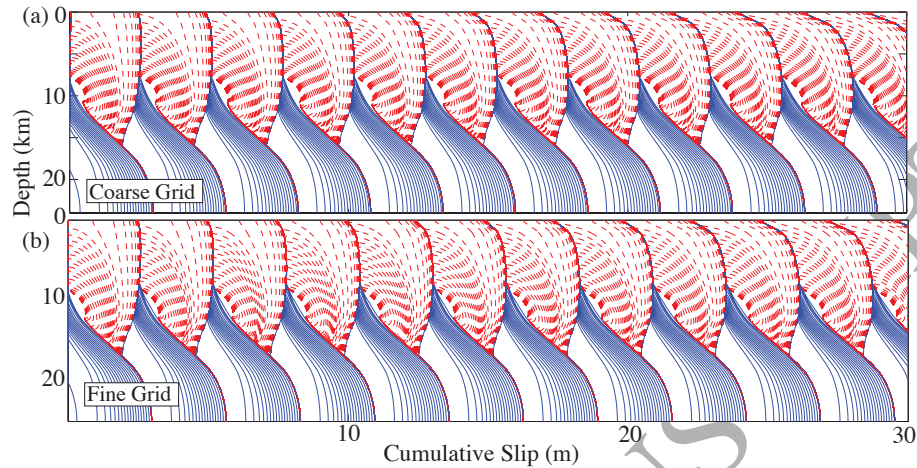


Figure C.14: Snapshots of cumulative slip profiles plotted at 5-s intervals during interseismic period when $\max(V) \leq 1$ mm/s and dashed red profiles plotted at 1 s intervals during quasi-dynamic rupture for $\eta = 36$ GPa-s, $h = 0$ GPa, $c = 50$ MPa for (a) the coarse grid simulation from Fig. 7(c) (plotted again for ease of comparison) and (b) results when using twice the number of grid points.

- 1042 Aagaard, B. T., Knepley, M. G. and Williams, C. A. (2013), A domain
 1043 decomposition approach to implementing fault slip in finite-element models
 1044 of quasi-static and dynamic crustal deformation, *J. Geophys. Res.*, **118**,
 1045 3059–3079, doi:10.1002/jgrb.50217
- 1046 Allison, K. L. and Dunham, E. M. (2016), Earthquake cycle simulations with
 1047 rate-and-state friction and nonlinear Maxwell rheology. *Tectonophysics*,
 1048 submitted.
- 1049 Ampuero, J.-P. and Rubin, A. M. (2008), Earthquake nucleation on rate
 1050 and state faults: Aging and slip laws, *J. Geophys. Res.*, **113**, B01302, doi:
 1051 10.1029/2007JB005082.
- 1052 Barbot, S., Lapusta, N. and Avouac, J.-P. (2012), Under the hood of the
 1053 earthquake machine: Toward predictive modeling of the seismic cycle, *Sci-*
 1054 *ence*, **336**, 707–710, doi:10.1126/science.1218796.
- 1055 Ben-Zion, Y. and Sammis, C. (2011), Brittle Deformation of Solid and Gran-
 1056 ular Materials with Applications to Mechanics of Earthquakes and Faults,
 1057 *Pure Appl. Geophys.*, **168**, 2147–2149, doi:10.1007/s00024-011-0418-8.

- 1058 Bower, A. F. (2010), Applied Mechanics of Solids, Taylor and Francis Group,
1059 LLC, CRC Press, Boca Raton, FL.
- 1060 Chen, W. F. and Han, D. J. (1988), *Plasticity for Structural Engineers*, first
1061 ed., Springer-Verlag, New York, 1–606.
- 1062 Chester, F. M., Evans, J. P. and Biegel, R. L. (1993), Internal structure
1063 and weakening mechanisms of the San Andreas fault, *J. Geophys. Res.*, **98**,
1064 771–786, doi:10.1029/92JB01866.
- 1065 Chester, F. M. and Logan, J. M. (1986), Implications for mechanical prop-
1066 erties of brittle faults from observations of the Punchbowl fault zone, Cal-
1067 ifornia, *Pure Appl. Geophys.*, **124**, 79–106 doi:10.1007/BF00875720.
- 1068 de Souza Neto, E. A., Perić, D. and Owen, D. R. J. (2008), *Computational*
1069 *Methods for Plasticity*, first ed., John Wiley & Sons Ltd, United Kingdom,
1070 1–791. DeSouza
- 1071 Dieterich, J. H. (1979), Modeling of rock friction: 1. Experimental results
1072 and constitutive equations, *J. Geophys. Res.*, **84**, 2161–2168, doi:10.1029/
1073 JB084iB05p02161.
- 1074 Drucker, D. C. (1959), A definition of a stable inelastic material, *J. Appl.*
1075 *Mech. ASME*, **26**, 101–195.
- 1076 Dunham, E. M., Belanger, D., Cong, L. and Kozdon, J. E. (2011a), Earth-
1077 quake ruptures with strongly rate-weakening friction and off-fault plastic-
1078 ity, Part 1: Planar faults, *Bull. Seismol. Soc. Am.*, **101**, 5, 2296–2307,
1079 doi:10.1785/0120100075.
- 1080 Dunham, E. M., Belanger, D., Cong, L. and Kozdon, J. E. (2011b), Earth-
1081 quake ruptures with strongly rate-weakening friction and off-fault plastic-
1082 ity, Part 2: Nonplanar faults, *Bull. Seismol. Soc. Am.*, **101**, 5, 2308–2322,
1083 doi:10.1785/0120100076.
- 1084 Dunne, F. and Petrinic, N. (2006), *Introduction to Computational Plasticity*,
1085 first ed., Oxford University Press, New York, 1–242.
- 1086 Duru, K. and Virta, K. (2014), Stable and high order accurate difference
1087 methods for the elastic wave equation in discontinuous media, *J. Comp.*
1088 *Phys.*, **279**, 37–62, doi:10.1016/j.jcp.2014.08.046.

- 1089 Erickson, B. A., and Dunham, E. M. (2014), An efficient numerical method
 1090 for earthquake cycles in heterogeneous media: Alternating subbasin and
 1091 surface-rupturing events on faults crossing a sedimentary basin, *J. Geophys.*
 1092 *Res.*, **119**, 1–27, doi:10.1002/2013JB010614.
- 1093 Faulkner, D. R., Jackson, C. A. L., Lunn, R. J., Schlische, R. W., Shipton, Z.
 1094 K., Wibberley, C. A. J. and Withjack, M. O. (2010), A review of recent
 1095 developments concerning the structure, mechanics and fluid flow properties
 1096 of fault zones, *J. Struct. Geol.*, **32**, 11, 1557–1575, doi:10.1016/j.jsg.2010.
 1097 06.009.
- 1098 Gabriel, A.-A., Ampuero, J.-P., Dalguer, L. A. and Mai, P. M. (2013), Source
 1099 properties of dynamic rupture pulses with off-fault plasticity, *J. Geophys.*
 1100 *Res.*, **118**, 8, 4117–4126, doi:10.1002/jgrb.50213.
- 1101 Gabriel, A.-A., Ampuero, J.-P., Dalguer, L. A. and Mai, P. M. (2013),
 1102 The transition of dynamic rupture styles in elastic media under
 1103 velocity-weakening friction, *J. Geophys. Res.*, **117**, B09311, doi:10.1029/
 1104 2012JB009468.
- 1105 Glowinski, R., and Le Tallec, P. (1989), Augmented Lagrangian and Opera-
 1106 tor Splitting Methods in Nonlinear Mechanics, Society for Industrial and
 1107 Applied Mathematics, Philadelphia, Volume 9.
- 1108 Golub, G. H. and Van Loan, C. F. (2013), Matrix Computations, 4th edition,
 1109 JHU press, Baltimore.
- 1110 Gustafsson, B. (2008), High Order Difference Methods for Time Dependent
 1111 PDE, Springer-Verlag, Berlin, doi:10.1007/978-3-540-74993-6.
- 1112 Horn, R. A. and Johnson, C. R. (1985), Matrix Analysis, Cambridge Univer-
 1113 sity Press, New York.
- 1114 Jain, S. K. (2008), Introduction to Theories of Plasticity, Part 1: Stress-
 1115 Strain Relations, Engineering Publications, Virginia.
- 1116 Johnson, K. M. and Segall, P. (2004), Viscoelastic earthquake cycle mod-
 1117 els with deep stress-driven creep along the San Andreas fault system, *J.*
 1118 *Geophys. Res.*, **109**, B10403, doi:10.1029/2004JB003096.

- 1119 Kaneko, Y., Ampuero, J.-P. and Lapusta, N. (2011), Spectral-element simu-
 1120 lations of long-term fault slip: Effect of low-rigidity layers on earthquake-
 1121 cycle dynamics, *J. Geophys. Res.*, **116**, B10313, 1–18, doi:10.1029/
 1122 2011JB008395.
- 1123 Kaneko, Y., and Fialko, Y. (2011), Shallow slip deficit due to large strike-slip
 1124 earthquakes in dynamic rupture simulations with elasto-plastic off-fault
 1125 response, *Geophys. J. Int.*, **186**, 1389–1403, doi:10.1111/j.1365-246X.2011.
 1126 05117.x.
- 1127 Kozdon, J. E., Dunham, E. M. and Nordström, J. (2012), Interaction of waves
 1128 with frictional interfaces using summation-by-parts difference operators:
 1129 Weak enforcement of nonlinear boundary conditions, *J. Sci. Comput.*, **50**,
 1130 341–367, doi:10.1007/s10915-011-9485-3.
- 1131 Kreiss, H.-O. and Scherer, G. (1974), Finite element and finite difference
 1132 methods for hyperbolic partial differential equations, *Mathematical aspects*
 1133 *of finite elements in partial differential equations*, Academic Press, Inc.,
 1134 195–212, doi:10.1016/B978-0-12-208350-1.50012-1.
- 1135 Kreiss, H.-O. and Scherer, G. (1977), On the existence of energy estimates for
 1136 difference approximations for hyperbolic systems, *Technical Report*, Dept.
 1137 of Scientific Computing, Uppsala University.
- 1138 Lapusta, N., Rice, J. R., Ben-Zion, Y. and Zheng, G. (2000), Elastodynamic
 1139 analysis for slow tectonic loading with spontaneous rupture episodes on
 1140 faults with rate-and-state dependent friction, *J. Geophys. Res.*, **105**, 23765–
 1141 23789, doi:10.1029/2000JB900250.
- 1142 Ma, S. and Andrews, D. J. (2010), Inelastic off-fault response and three-
 1143 dimensional earthquake rupture dynamics on a strike-slip fault, *J. Geo-
 1144 phys. Res.*, **115**, B04304, doi:10.1029/2009JB006382.
- 1145 Marone, C. (1998), Laboratory-derived friction laws and their application to
 1146 seismic faulting, *Annu. Rev. Earth Planet. Sci.*, **26**, 643–696, doi:10.1146/
 1147 annurev.earth.26.1.643.
- 1148 Mattsson, K. (2011), Summation by parts operators for finite difference ap-
 1149 proximations of second-derivatives with variable coefficients, *J. Sci. Com-
 1150 put.*, **51**, 650–682, doi:10.1007/s10915-011-9525-z.

- 1151 Mattsson, K. and Nordström, J. (2004), Summation by parts operators for
 1152 finite difference approximations of second derivatives, *J. Comput. Phys.*,
 1153 **199**, 503–540, doi:10.1016/j.jcp.2004.03.001.
- 1154 Mattsson, K., Ham, F. and Iaccarino, G. (2008), Stable and accurate wave-
 1155 propagation in discontinuous media, *J. Comput. Phys.*, **227**, 8753–8767
 1156 doi:10.1016/j.jcp.2004.03.001.
- 1157 Mazzoni, S., McKenna, F., Scott, M. H., and Fenves, G. L., (2009), Open
 1158 system for earthquake engineering simulation user manual. University of
 1159 California, Berkeley.
- 1160 Meade, B. J., Klinger, Y., and Hetland, E. A., (2013), Inference of multiple
 1161 earthquake-cycle relaxation timescales from irregular geodetic sampling of
 1162 interseismic deformation, *Bull. Seismol. Soc. Am.*, **103**, 2824–2835 doi:
 1163 10.1785/0120130006.
- 1164 Mitchell, T. M. and Faulkner, D. R. (2009), The nature and origin of off-fault
 1165 damage surrounding strike-slip fault zones with a wide range of displace-
 1166 ments: A field study from the Atacama fault zone, northern Chile, *J.*
 1167 *Struct. Geol.*, **31**, 8, 802–816, doi:10.1016/j.jsg.2009.05.002.
- 1168 Nordström, J., Mattsson, K. and Swanson, C. (2007), Boundary conditions
 1169 for a divergence free velocity-pressure formulation of the Navier-Stokes
 1170 equations, *J. Comput. Phys.*, **225**, 874–890, doi:10.1016/j.jcp.2007.01.010.
- 1171 Perzyna, P. (1966), Fundamental Problems in Viscoplasticity, *Advances*
 1172 *in Applied Mechanics*, **9**, 243 - 377, doi:http://dx.doi.org/10.1016/
 1173 S0065-2156(08)70009-7.
- 1174 Perzyna, P. (1971), Thermodynamic Theory of Viscoplasticity, *Advances*
 1175 *in Applied Mechanics*, **11**, 313 - 354, doi:http://dx.doi.org/10.1016/
 1176 S0065-2156(08)70345-4.
- 1177 Power, W. L and Tullis, T. E. (1991), Euclidean and fractal models for the
 1178 description of rock surface roughness, *J. Geophys. Res.*, **96**, B1, 415–424,
 1179 doi:10.1029/90JB02107.
- 1180 Ranjith, K. (2008), Dynamic anti-plane sliding of dissimilar anisotropic
 1181 linear elastic solids, *Int. J. Solids Struct.*, **45**, 4211–4221, doi:10.1016/j.
 1182 ijsolstr.2008.03.002.

- 1183 Rice, J. R. (1992), Fault stress states, pore pressure distributions and the
1184 weakness of the San Andreas fault, in *Fault Mechanics and Transport Prop-*
1185 *erties of Rock*, edited by Evans, B. and Wong, T.-F., 475 – 503, Academic,
1186 San Diego, Calif.
- 1187 Rice, J. R. (1993), Spatio-temporal complexity of slip on a fault, *J. Geophys.*
1188 *Res.*, **98**, 9985–9907, doi:10.1029/93JB00191.
- 1189 Roache, P. (1998), *Verification and Validation in Computational Science and*
1190 *Engineering*, first ed., Hermosa Publishers, Albuquerque.
- 1191 Roten, D., Olsen, K. B., Day, S. M. and Cui, Y. (2016), Quantification of
1192 fault zone plasticity effects with spontaneous rupture simulations, *Work-*
1193 *shop on Best Practices in Physics-Based Fault Rupture Models for Seismic*
1194 *Hazard Assessment of Nuclear Installations*, 18–20 November 2015, Vi-
1195 enna, Unpublished conference paper.
- 1196 Ruina, A. (1983), Slip instability and state variable friction laws, *J. Geophys.*
1197 *Res.*, **88**, B12, 10359–10370, doi:10.1029/JB088iB12p10359.
- 1198 Scalerandi M., Delsanto, P. P., Chiroiu, C. and Chiroiu, V. (1999), Numerical
1199 simulation of pulse propagation in nonlinear 1-D media, *J. Acoust. Soc.*
1200 *Am.*, **106**, doi:10.1121/1.428078.
- 1201 Shi, Z. and Day, S. M. (2013), Rupture dynamics and ground motion from 3-
1202 D rough-fault simulations, *J. Geophys. Res.*, **118**, 1122–1141, doi:10.1002/
1203 jgrb.50094.
- 1204 Shipton, Z. K., Evans, J. P. and Thompson, L. B. (2005), The geometry
1205 and thickness of deformation-band fault core and its influence on sealing
1206 characteristics of deformation-band fault zones, in *Faults, Fluid Flow, and*
1207 *Petroleum Traps*, AAPG Mem., **85**, edited by R. Sorkabi and Y. Tsuji,
1208 181–195, American Association of Petroleum Geologists, Tulsa, Okla.
- 1209 Simo, J. C. and Taylor, R. L. (1985), Consistent tangent operators for rate-
1210 independent elastoplasticity, *Comput. Methods Appl. Mech. Eng.*, **48**, 101–
1211 118, doi:10.1016/0045-7825(85)90070-2.
- 1212 Simo, J. C. and Hughes, T. J. R. (1998), *Computational Inelasticity*, first
1213 ed., Springer, New York, doi:10.1007/b98904.

- 1214 Svärd, M. and Nordström, J. (2014), Review of summation-by-parts schemes
1215 for initial-boundary-value problems, *J. Comput. Phys.*, **268**, 17–38, doi:
1216 10.1016/j.jcp.2014.02.031.
- 1217 Templeton, E. and Rice, J. R. (2008), Off-fault plasticity and earthquake
1218 rupture dynamics: 1. Dry materials or neglect of fluid pressure changes, *J.*
1219 *Geophys. Res.*, **113**, B09306, doi:10.1029/2007JB005529.
- 1220 Thompson, T. B. and Meade, B. J. (2016), Next generation boundary element
1221 models for earthquake science, Poster Presentation at 2016 SCEC Annual
1222 Meeting.
- 1223 Tullis, T. E., Richards-Dinger, K., Barall, M., Dietrich, J. H., Field, E. H.,
1224 Heien, E. M., Kellog, L. H., Pollitz, F. F., Rundle, J. B., Sachs, M. K., Tur-
1225 cotte, D. L., Ward, S. N. and Yikilmaz, M. B. (2012), Generic earthquake
1226 simulator, *Seismol. Res. Lett.*, **83**, 959–963, doi:10.1785/0220120093.
- 1227 Virta, K. and Mattsson, K. (2014), Acoustic wave propagation in complicated
1228 geometries and heterogeneous media, *J. Sci. Comput.*, **61**, doi:10.1007/
1229 s10915-014-9817-1.
- 1230 Xu, S., Ben-Zion, Y. and Ampuero, J.-P. (2012), Properties of inelas-
1231 tic yielding zones generated by in-plane dynamic ruptures: I. Model
1232 description and basic results, *Geophys. J. Int.*, **191**, 1325–1342, doi:
1233 10.1111/j.1365-246X.2012.05679.x.
- 1234 Xu, S., Ben-Zion, Y. and Ampuero, J.-P. (2012), Properties of inelastic yield-
1235 ing zones generated by in-plane dynamic ruptures: II. Detailed parameter-
1236 space study, *Geophys. J. Int.*, **191**, 1343–1360, doi:10.1111/j.1365-246X.
1237 2012.05685.x.